FULL SCALE TRAIN UNDERBODY AERODYNAMIC EVALUATION FOR TOP OF RAIL FRICTION MODIFER APPLICATION

by

Quinn Alexander Mulligan

B.Eng., Carleton University, 2012

A THESIS SUBMITTED IN PARTIAL FULFULLIMENT OF

THE REQUIREMENTS FOR THE DEGREE OF

MASTER OF APPLIED SCIENCE

in

The Faculty of Graduate and Postdoctoral Studies

(Mechanical Engineering)

THE UNIVERSITY OF BRITISH COLUMBIA

(Vancouver)

April 2015

ABSTRACT

Liquid jet impingement is employed in the rail industry to apply friction modifier to the rail surface. Use of the friction modifier is known to reduce wear and improve fuel efficiency. L.B. Foster ® deploys friction modifier using a nozzle located downwind of the wheels on freight trains. Understanding the aerodynamic environment of the nozzle is important for researching how to maximize the deposition of the liquid friction modifier from the nozzle to the tracks.

The air pressure and velocity at the location of the nozzle was evaluated experimentally at full scale in field trials. The pressure at a fixed ground location was measured by transducers as the train passed. The air velocity in the reference frame of the moving vehicle was measured using a fiber-film anemometer at the location of the liquid-friction-modifier spray nozzle, 0.4 wheel diameters downwind of the wheel center.

The measured air speeds scales linearly with the train speed, and the measured pressure scales linearly with the dynamic pressure, implying that Reynolds number effects are negligible. The pressure distribution showed an initial pressure increase just downwind of the leading edge of the vehicle followed by a spike in suction. The pressure distribution was found to depend on the orientation of the vehicle. With a rail car leading the vehicle, the spike in suction produced was about 50% larger than the suction spike produced when a locomotive, lower to the ground, was leading the vehicle.

The mean air speed was measured to be approximately 29% of the train speed. The mean air speed the same distance upwind of the wheel was measured to be approximately 38% of the train speed. Turbulence intensity levels were measured to be about 0.15. Cross wind effects became much less significant when the train speed was equal to or greater than the cross wind speed.

The train undercarriage airflow was modeled numerically using Autodesk Simulation CFD™ software. The CFD simulations were in approximate agreement (typically, within 2%) with experimental measurements and confirmed that the presence of the support bracket for the anemometer had limited impact on the measured wind speed.

PREFACE

This dissertation is original, unpublished work. The hardware used was purchased from respective companies as specified when mentioning each component and part number. The bracket apparatus designed in Chapter 2 was created by the author, Quinn Mulligan.

The authors of Chapter 2 are Quinn Mulligan and Dr. Sheldon Green. Dr. Green proposed methods to practice and prepare for the experimental work performed in Chapter 3.

The authors of Chapter 3 are Quinn Mulligan and Dr. Sheldon Green. Dr. Green, as well as representatives from LB Foster(R), identified the requirement to characterize the aerodynamic environment in order to better understand the input parameters for liquid jet impingement outside of the characteristics of the jet itself.

The authors of Chapter 4 are Quinn Mulligan and Dr. Sheldon Green. Dr. Green suggested further characterization of the aerodynamic region of interest by performing simulations based on the boundary conditions found experimentally in Chapter 3.

TABLE OF CONTENTS

LIST OF TABLES

LIST OF FIGURES

LIST OF SYMBOLS

v	Velocity [m s^{-1}]
V	Voltage [V]
f	Vortex shedding frequency [Hz]
D	Diameter [m]
St	Strouhal number
Re	Reynolds number
ν	Kinematic viscosity [m^2 s^{-1}]
C_P	Pressure coefficient
P	Pressure [N m^{-2}]
ρ	Density [kg m^{-3}]
τ	Characteristic time [s]
t	Time [s]
l	Length [m]
L	Characteristic length [L]
$\propto$	Rotational velocity
ω	Rotation speed [Hz]

ACKNOWLEDGEMENTS

I wish to thank my supervisor, Dr. Sheldon Green, for providing excellent guidance, advice, and mentorship while I completed this thesis work. Having Dr. Green's knowledge, experience, and enthusiasm was an invaluable resource and assisted greatly in working towards the completion of this project. It was always fun to see how many significant figures of the constants in formulas describing relevant fluid flows Dr. Green could recall just from memory. It was also fascinating to see Dr. Green estimate nozzle orifice sizes on the order of several hundred microns, just by eyeballing it, with remarkable accuracy.

I would also like to acknowledge the students in my research group: Yuchen Guo, Alireza Sarraf, Hatef Rahmani and Morgan Hibbert. Together with Dr. Green, our weekly meetings were always a fun way to discuss our work and brainstorm ideas for the following weeks.

Thank you to our sponsor company, L.B. Foster®, for making this work possible. In particular, thank you to Dave Elvidge, Don Eadie and John Cotter for all of your advice and support. An extended thank you to Dave for facilitating our trip through Denver and really making sure it was productive and fun. Thank you for letting me ride in the cabin of the locomotive while you had to watch us roll by!

Finally, I also wish to thank Dr. John Dabiri, Dr. Matthias Kinzel and Dr. Julia Cosse for providing me with great guidance and helping me to develop into a research engineer.

DEDICATION

I dedicate this work to Aalysia. When I began my work at the University of British Columbia, she was Aalysia Colyn. As I finish this work, she is now Aalysia Mulligan. I cannot thank my loving and supporting wife enough for being with me through every situation, enduring early mornings and late nights while I worked towards completing my thesis, and listening to me try to explain what exactly I’m doing over and over again.

1 INTRODUCTION

Proper friction management on railroad tracks reduces slipping at the wheel-rail interface and thus improves the efficiency of train operation. Liquid jet impingement and air blast atomization is being considered by LB Foster® as a means to apply friction modifier to the rail surface. In the case of air blast atomization, fine droplets of liquid friction modifier are carried by high speed air from the underbody nozzle to the rail surface. Similarly, in the case of liquid jet impingement, a high-speed jet of non-Newtonian liquid friction modifier is shot from a nozzle located at the underbody of a rail car with the intention of applying a thin-film to the rail surface. Figure 1-1 sketches the scenario for LB Foster®'s liquid jet impingement problem. On the left, a column of liquid is deployed to the rail which moves relative to the nozzle. On the right, the same column of liquid is exposed to an aerodynamic environment, as it would in practice, in which the jet is deflected. In order to understand the environment in which the product can be deployed, it is essential to qualitatively and quantitatively understand the pressure and velocity distribution of the air between the nozzle and the lamella of the impinging jet at the rail surface.

Figure 1-1 Liquid jet impingement diagram

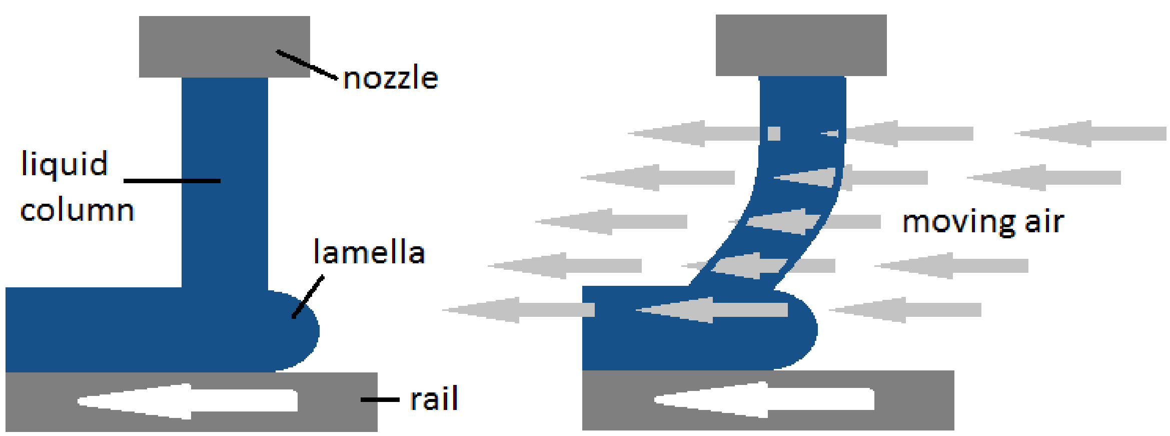

This research experimentally evaluates a full-scale freight train at operating conditions. To quantify the underbody velocity field, a fiber-film hot wire anemometer was mounted to the vehicle and employed to measure the air velocity distribution in the vicinity of the nozzle dispensing said friction modifier. To quantify the underbody pressure field, an array of ground-born pressure transducers were employed to measure the air pressure as the vehicle passed by. These methods were used to examine conditions with different underbody geometries depending on the vehicle orientation. The results of the research will be applicable to trains travelling at any speed as the flow fields are scalable with velocity. In particular, there is novelty in the interrogation of the air flow at the underbody of a moving vehicle directly behind a rotating wheel and the research will be used in industrial applications beyond rail cars such as braking and automobile traction control. The goal of the research is to assist in the engineering of the optimal conditions for liquid friction modifier to be applied to a rail surface producing maximum fuel efficiency and minimum maintenance costs for train operation.

Understanding the state of the art at which the characteristics of liquid jet impingement on a moving surface has been evaluated by previous work. It is necessary to review literature on train aerodynamics to provide necessary knowledge as well as to understand which experimental methods have been successful and what has not been studied in previous work. Velocity and pressure fields behind a rotating wheel at the underbody of a moving freight train at full scale have never been experimentally measured.

1.1 Jet Impingement

The Applied Fluid Mechanics Laboratory at the University of British Columbia has previously conducted research investigating the impingement of a liquid jet on a moving surface. Moulson [1] concluded that the outcome of the jet's lamella splashing or depositing on the surface depends on the viscosity of the fluid, the impingement angle, the speed of the jet, and the speed of the surface. It was also determined that the surrounding air pressure affects the onset of splashing. Moulson determined that deposition will occur at low and high pressure, i.e. there exists a range of pressure where splashing of the lamella is present. The splashing is caused by lamella detachment due to aerodynamic forces acting on the leading edge disrupting the stability of the surface tension and fluid pressure balance. Moulson also determined that lamella detachment depends on the Reynolds number of the liquid jet.

Sterling [2] discovered that, though a lamella may detach from a moving surface, recovery to deposition will eventually occur. The recovery time was found to be a stochastic process with higher surface roughness having a higher probability of a faster recovery time.

Sterling also determined that a large impingement angle of a jet resulting from a fast cross wind, i.e. a jet that has been deflected by a cross wind to a non-perpendicular angle, is more prone to deposition and less prone to splashing. Sterling suggests further investigation of the aerodynamic conditions that exist in the vicinity of a liquid jet.

1.2 Train Aerodynamics

Several studies that have been performed on the aerodynamics of high speed trains were compiled by Baker [3], in particular the bullet trains in South Korea. Baker presented research investigating the aerodynamics near the nose of the train, the boundary layers on the side and roof of the train, and, of particular interest, the aerodynamics at the underbody of the train.

Baker [3] states that, as the nose of the train becomes increasingly blunt, as represented by a freight train, an increasing disturbance is found downwind in the velocity and pressure fields. These results were found using conventional trackside anemometry.

The boundary layer on the side walls of the train was determined at full scale and in a wind tunnel setting as presented by Baker [3]. Previous experiments have shown that boundary layer parameters such as displacement thickness, i.e. the length that a surface would be moved to produce the same flow rate in inviscid flow, and the skin friction coefficient, i.e. the ratio between the wall shear stress and the dynamic pressure in the flow, can be found using pitot tubes or hot wire anemometers – however, hot wire anemometers allow for a much higher sample rate and can capture the turbulence intensity of the flow. Baker [3] states that results from full scale testing differ from the results from wind tunnel testing. It is suggested that the differences are due to the dependence of skin friction coefficient on the scale. Steady growth of boundary layer thickness and displacement thickness along the length was observed in wind tunnel testing but was not present in full scale testing.

Research investigating the boundary layer on the train roof was also performed and presented by Baker [3]. Compared to the boundary layer development on the side walls, the boundary layer on the roof is much thicker. The suggestion is this is because of rapid growth of the boundary layer near the nose due to flow separation. Each situation presented by Baker suggests a typical logarithmic velocity distribution, i.e. by the law of the wall in for turbulent boundary layer as presented by Bradshaw [4] and Kinzel [5]. Itoh [6] used laser-doppler velocimetry to study the velocity field in a turbulent boundary layer to further confirm the concept of the logarithmic velocity distribution.

Of particular interest to the research project is the aerodynamic assessment of the train underbody flow. Baker [3] presents results motivated by ballast flying, i.e. the lift of the ballast underneath the tracks due to aerodynamic effects. Pitot tubes were mounted to a train to measure the mean air speed at 0.5 wheel diameters above the rail in the vehicle's reference frame. At this height, it was concluded that the air speed was 40% of the train speed. The wind speed is slower closer to the tracks in comparison to the centerline of the train. However, because of the non-slip condition of the train underbody, the ground, and the rails, a non-conventional boundary layer profile exists, i.e. the expected logarithmic velocity distribution suggested by Bradshaw [5] and Kinzel [6] of a turbulent boundary layer is not present. Baker [3] suggests that, due to the challenging nature of collecting experimental data in such a hazardous environment, as well as the complexity of modelling the turbulence for computational analysis, the opportunity exists for to future work developing a novel way to characterize underbody air flow.

Air speed testing near the underbody of a full scale freight train was performed by L.B. Foster ® and suggested that, as the train speed increases, the air speed approximately one wheel diameter away from the side of the train at the height of the underbody increases at approximately the same rate, as to be expected. However, it was found by Elvidge [7] that the direction of the air velocity, even in naturally windy conditions, is in the direction of the train.

It is a hypothesis that the turbulence in the surrounding air could be a factor in the stochastic characteristics of lamella detachment recovery found by Sterling [2].

1.3 Research Objectives

The principal objective of the research is to complete an experimental aerodynamic assessment at the underbody of a freight train at operating conditions. To achieve this, the following objectives were outlined:

1. To quantify the air pressure distribution near the ground as a full scale freight-train passes overhead.
2. To quantify the air velocity distribution in the vicinity of a train wheel of a full scale freight-train.
3. To compare experimental results with computationally predicted results to help build a model which can provide data for all situations without the expense of performing on-site experiments.

2 METHODS

Performing full-scale experimentation on a freight train requires a locomotive, rail car, crew with an engineer to drive the locomotive, a stretch of uninterrupted track, and a well thought-out test procedure in order to be able to perform all types of testing within the allotted time frame. There is no way to replicate the test conditions exactly, i.e. mounting fragile sensors to a train while accounting for vibrations and debris, but it is still essential to perform practice runs to best prepare and make the most of time on-site.

There are three main components required to gather the data required to perform the experimental aerodynamic analysis. A weather station records ambient conditions. A fiber-film hot-wire anemometer is mounted to the train and captures air velocities in the reference frame of the moving vehicle. An array of pressure transducers, mounted to the track, measures the air pressure as the vehicle passes over. A block diagram for the experimental set up is shown in Figure 2-1.

Figure 2-1 Block diagram for experimental setup

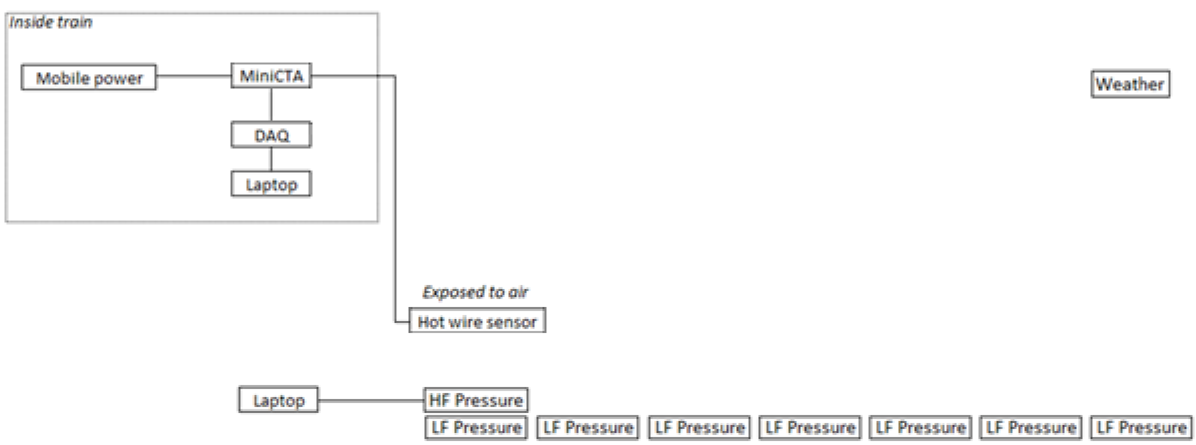

Each of the components in the experimental setup required extensive testing to ensure their viability, practicality, and robustness. Without access to an actual train, the components were all tested in a laboratory setting, a wind tunnel setting, and mounted to an automobile to best replicate conditions when mounted to a train. Section 2.1 outlines the preparation completed prior to on-site experimentation. Section 2.2 gives an overview of the tracking of ambient conditions. Section 2.3 explains the sensors used to monitor air pressure in the reference frame of the ground, and section 2.4 explains how the air velocity was captured in the reference frame of the vehicle.

2.1 Preparation for On-Site Testing

Each component in the experimental setup was first tested individually in a laboratory environment, in a wind tunnel, and mounted to an automobile for preliminary testing as a unit. The fiber-film hot wire anemometers required calibration as outlined in section 2.1.1.

2.1.1 **Calibration for Hot Wire Anemometers**

Fiber-film hot wire anemometers from Dantec Dynamics, part number 9055R0021, were selected to measure air velocity. Hot wire anemometry was chosen to measure air velocity due to its ability to acquire a high resolution of velocity data with a high sample rate, and its ability to capture near instantaneous fluctuations with a fast response time. In these experiments, the sample rate was 1 kHz. To satisfy the Nyquist Theorem, the fastest allowable frequency component would be 500 Hz. Based on the Strouhal and Reynolds numbers for comparable shapes (e.g., Ahlborn [8]), as well as the velocity envelope of the experimental conditions, the minimum allowable characteristic length, which would shed a von Karman vortex street at a rate of 500 Hz, would be 2 mm. This is considered to be acceptable, as the shapes that are of immediate interest, such as the wheel and nozzle bracket, are at least one order of magnitude larger. The wire was mounted perpendicularly to the track to capture the velocity component parallel with the track. The probes were mounted as sketched in Figure 2-2.

Figure 2-2 Orientation of hot wire anemometer

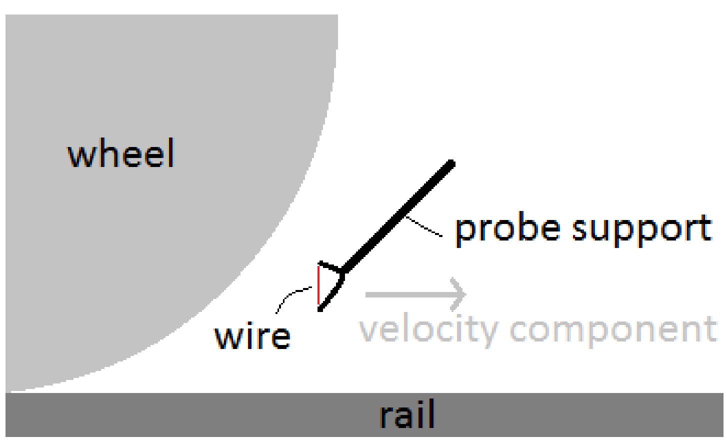

The probes are connected via cable to a Dantec Dynamics MiniCTA system, part number 9054T0421. The MiniCTA system controls the working temperature of the probe based on the overheat resistance, which is a function of properties including sensor resistance, leads resistance, sensor temperature coefficient of resistance, cable resistance, and the configurable MiniCTA decade resistance. The decade resistance can be found by defining an operating wire temperature. The MiniCTA is then connected to a mobile power source, a MotoMaster Eliminator Lead-Acid battery, part number 011-2002-8. The MiniCTA is also connected to a National Instruments four-channel data acquisition system, part number 9138A0261, which is then connected to a Microsoft Windows 8 computer running National Instruments LabVIEW via USB cable. Henceforth, the complete fiber-film hot wire anemometer assembly will be referred to as the 'Constant Temperature Anemometry (CTA) system'.

The suggested operating wire temperature for the sensors used in these experiments was 242 degrees Celsius. The wire is heated by an electrical current. The temperature of the wire is kept constant by a servo amplifier controlling the current and is independent of the cooling caused by the air flow. The voltage change over the wire is then a direct measure of velocity. As the wire on the CTA system is short and thin at 3 mm long and 5 µm in diameter, it has low thermal inertia and can respond to fluctuations in the air flow up to 175 kHz [9]. Qualitatively, the response of the hot wire anemometer can be seen in Figure 2-3. The leftmost plot shows a sudden increase in air velocity. The middle plot shows an oscillating air velocity, and the right plot shows an increasing air velocity.

Figure 2-3 Qualitative example output from a hot wire anemometer

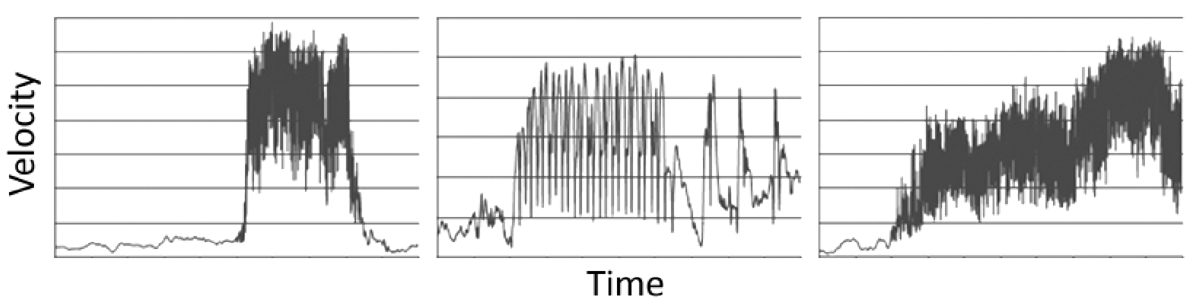

Though the voltage varies with the air velocity, the voltage is not proportional to air velocity – it is related by a regression fit recommended to be characterized by a fourth order polynomial. A probe needs to be calibrated by a recommended minimum of ten data points [9]. Figure 2-3 shows one CTA system sensor considered to be aerodynamically isolated, i.e. far from any walls or bodies which may interfere with the air flow, in the wind tunnel in the University of British Columbia's Rusty Hut building. The sensor itself is set at 45 degrees to the flow such that the wire is perpendicular to the flow, thus measuring the component of air velocity parallel with the walls.

The calibration results are shown in Figure 2-5. As predicted, a fourth order relationship exists between the measured voltage V and the free stream air velocity v. The free stream velocity for each data point is considered to be known, measured using pitot-static tubes mounted inside the wind tunnel. After use, performing the calibration again resulted in very little change to the curve on the order of tenths of a percent. The resulting empirical calibration curve was found to be:

$$v \left[\frac{\mathrm{m}}{\mathrm{s}}\right] \approx -0.8V^4 + 9.6V^3 - 31.6V^2 + 42.2V - 20.9 \tag{2.1}$$

Figure 2-4 Hot wire anemometer mounted in wind tunnel for calibration

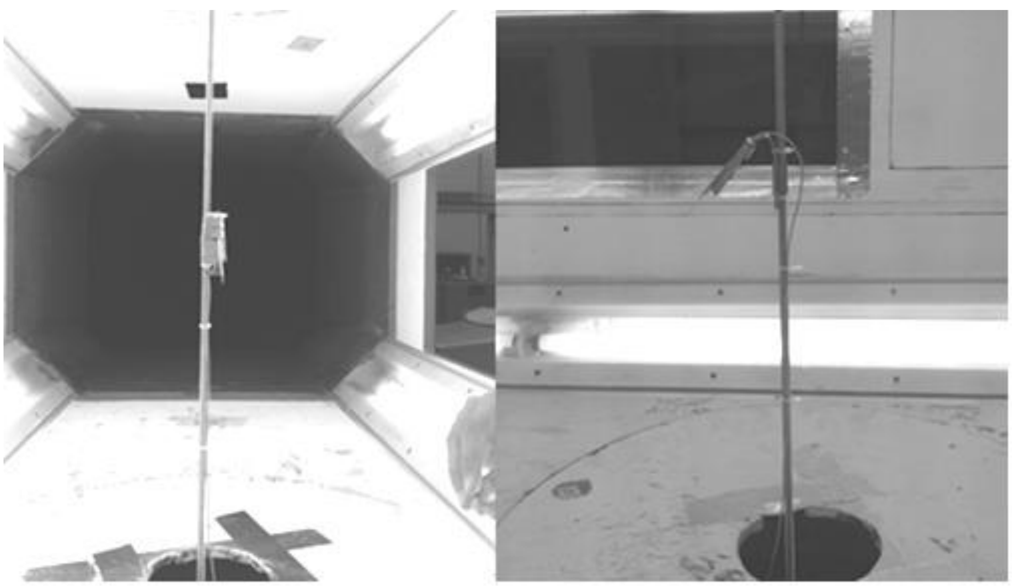

Figure 2-5 Calibration curve for hot wire anemometer

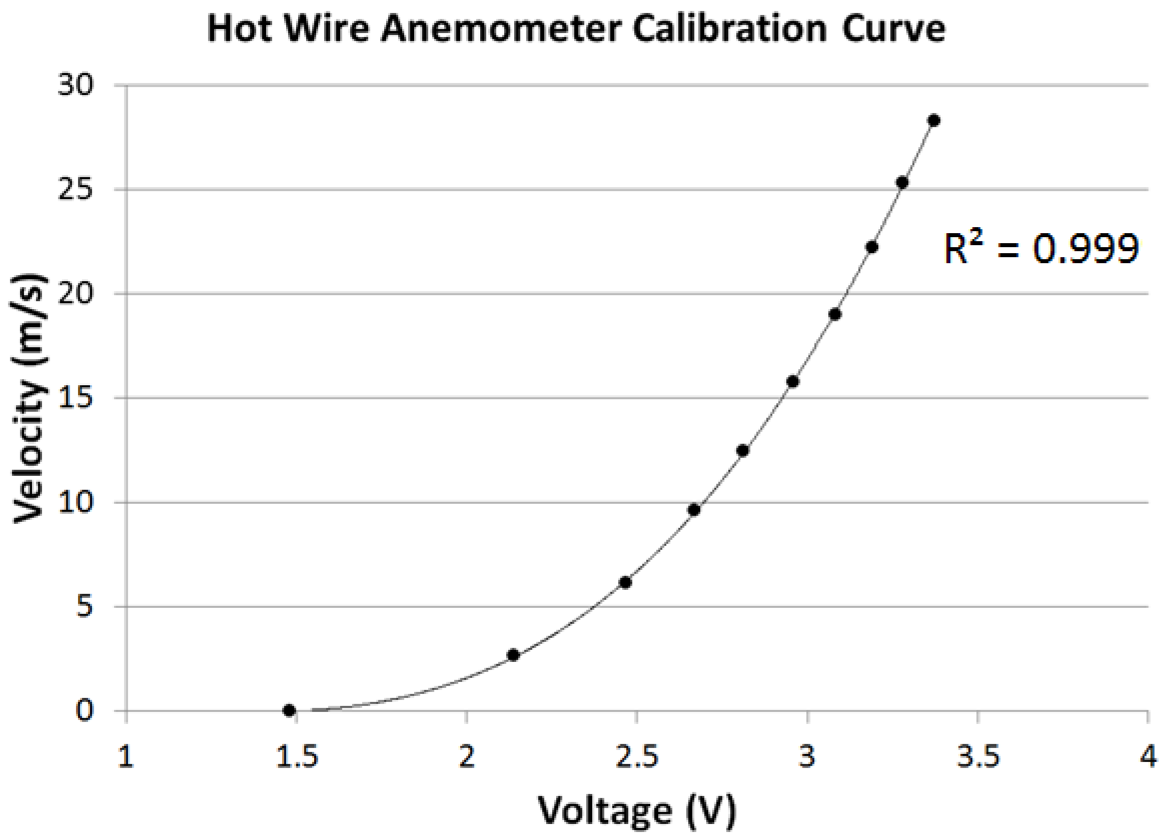

2.1.2 **Preliminary Car Testing**

In order to replicate the on-site experimental conditions, the CTA system was mounted to an automobile via flat brackets. This type of preliminary test allowed the CTA system to be tested as a mobile, self-sufficient unit, i.e. measuring air velocity in a moving vehicle while being completely mounted in the reference frame of the moving vehicle, as well as being subject to the vibrations experienced by a moving vehicle. Though the flow characteristics of the air are different than what is to be expected on-site, testing was done to verify the CTA system output for well-known conditions to best prepare for anticipated on-site conditions. The sensor was mounted ten characteristic length values away from the nearest body to measure free stream conditions. Figure 2-6 shows the free stream velocity output, i.e. the velocity of the uninterrupted air outside of the vehicle, recorded by the CTA system. Aside from the noise in the CTA system, a source of fluctuation that is experienced in this type of test that would not be present in a rail test would be the vibration of the vehicle due to the relatively large roughness scale of pavement compared to the top of rail.

Figure 2-6 Velocity at the free stream during car test

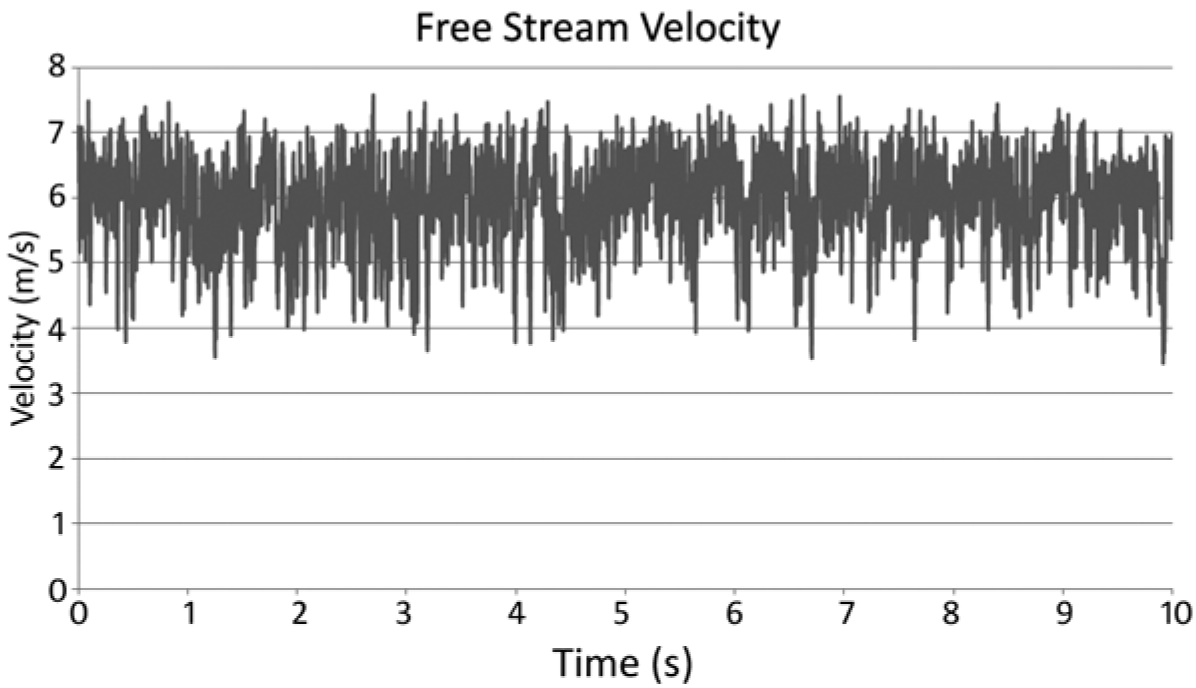

As the on-site experiments call for measuring the air velocity downwind of a body, i.e. a rotating wheel, it is expected vortices will be shed and thus need to be captured within the air velocity samples that are recorded. To produce a situation where vortices will be shed at a predictable rate, the side-view mirror of the automobile is used to replicate a cylindrical body. Figure 2-7 shows a well-known scenario of vortex shedding downwind of a cylinder with diameter D with air velocity v.

Figure 2-7 A sketch of a von Karman vortex street

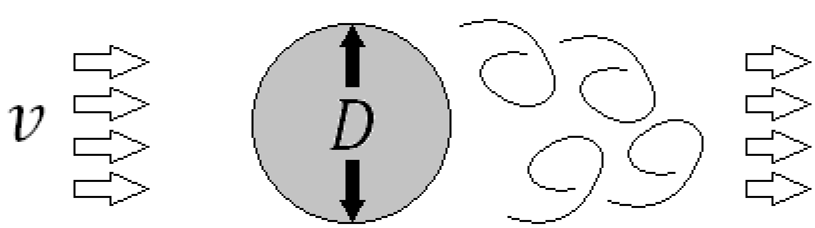

The vortex shedding frequency f is a function of air velocity v, cylinder diameter D, and the Strouhal number St. The Strouhal number, a dimensionless ratio of shedding speed to fluid speed, is a function of the Reynolds number Re and is typically $0.18 \leq St \leq 0.22$ for $10^2 \leq Re \leq 10^6$ for a cylinder. The Reynolds number, a dimensionless ratio of inertial forces to viscous forces, is a function of air velocity v, cylinder diameter D and fluid kinematic viscosity ν as in equation 2.2.

$$Re = \frac{vD}{\nu} \tag{2.2}$$

At the conditions of the automobile experiment, the free stream air velocity was measured to be $v_{fs} \approx 6\ \frac{\text{m}}{\text{s}}$ from Figure 2-6, the characteristic length, i.e. the width of the side-view mirror $D \approx 0.15$ m and kinematic viscosity $\nu = 1.51 \text{ x } 10^{-5}\ \frac{\text{m}^2}{\text{s}}$. Thus, the Reynolds number $10^2 \leq Re \approx 6 \text{ x } 10^4 \leq 10^6$ and it is then to be expected that the Strouhal number $0.18 \leq St \leq 0.22$. The Strouhal number St is defined by equation 2.3.

$$St = \frac{fD}{v_{fs}} \tag{2.3}$$

As the free stream air velocity v_{fs} and characteristic length D are known, and the vortex shedding frequency f can be found by analyzing the instantaneous, i.e. high sample-rate, air velocity. The air velocity was evaluated at one characteristic length downwind of the side-view mirror, i.e. 0.15 m downwind of the body. The results of this measurement are shown in Figure 2-8. The dominant frequencies in the velocity measurements can be found by performing a fast Fourier transform on the velocity data. Figure 2-9 shows the results of performing a fast Fourier transform of window size 4096 on the velocity measurements from Figure 2-8.

Figure 2-8 Velocity at one diameter downwind of side-view mirror during car test

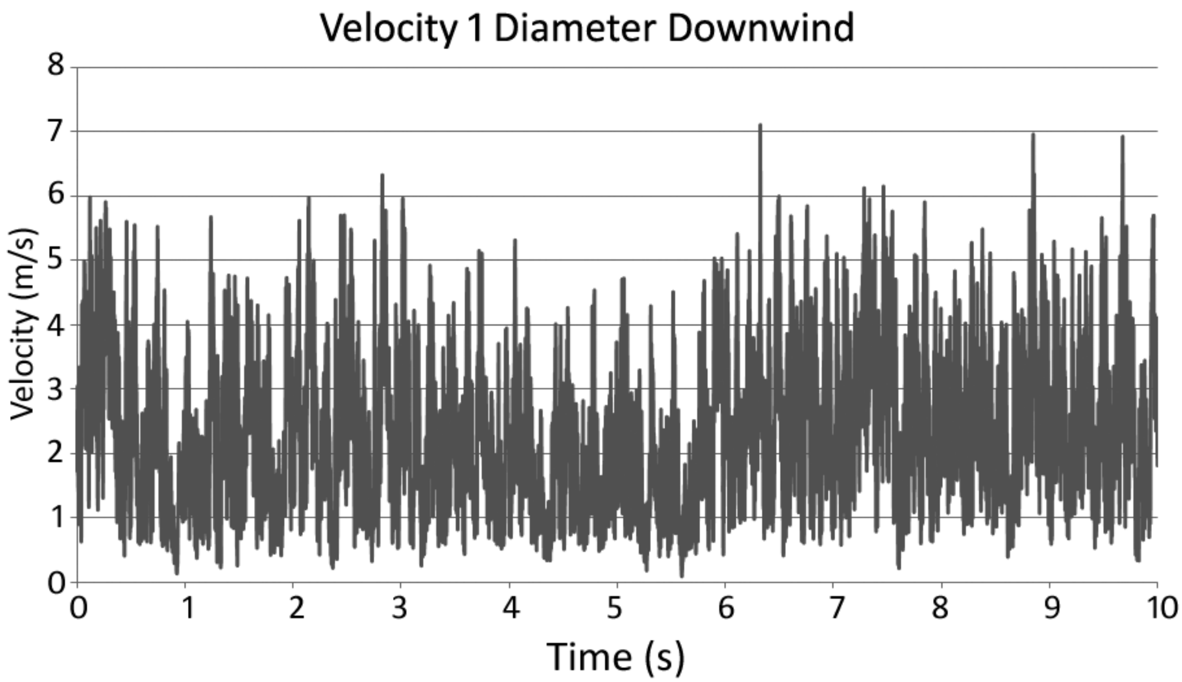

Figure 2-9 Fast Fourier transform of velocity downwind of side-view mirror for car test

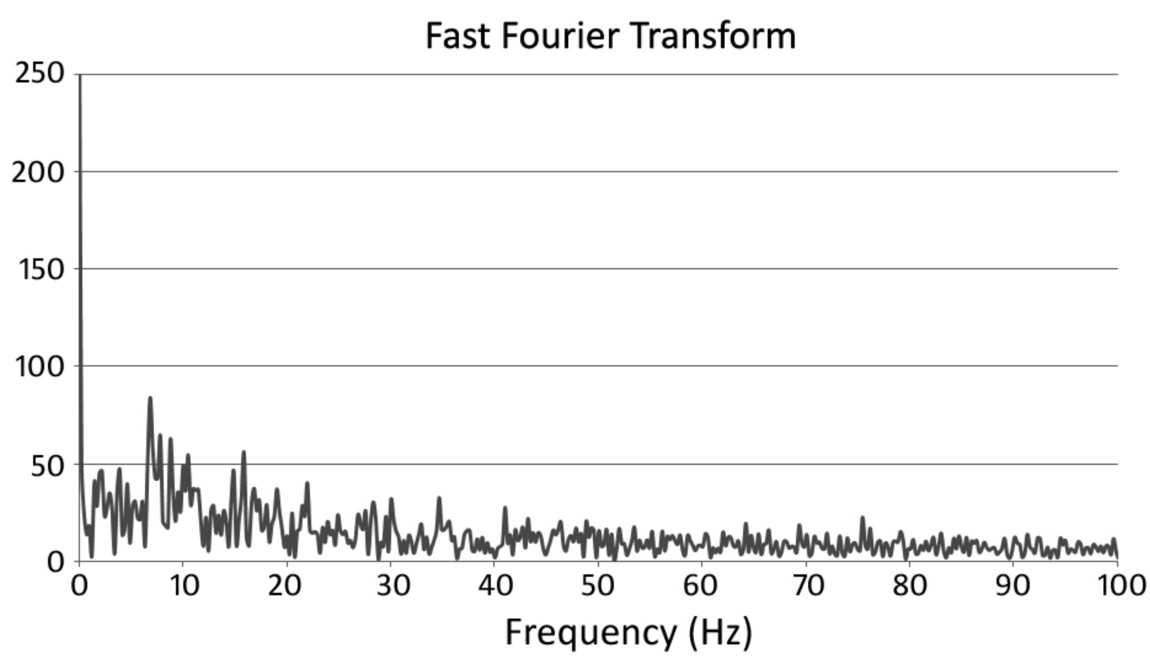

For equation 2.3 to be valid, i.e. for Strouhal number $0.18 \leq St \leq 0.22$, the vortex shedding frequency must be 7.2 Hz $\leq f \leq 8.8$ Hz. Figure 2-9 clearly shows dominant frequencies in this region, i.e. the magnitudes of the frequencies are high in the expected range of frequencies, thus demonstrating the capabilities of the CTA system capturing vortex shedding. The uncertainty in the dominant frequencies found using the fast Fourier transform, i.e. the reason there is a range of dominant frequencies rather than a single dominant frequency, can be attributed to the fact that the flow around the side-view mirror is three-dimensional, whereas equation 2.3, though it provides a good estimate, is actually for two-dimensional flow.

A series of pressure transducers were used to measure air pressure. The probes were mounted on the ground, thus measuring the static pressure as the vehicle passes over top of it in the reference frame of the ground. It is expected that the magnitude of the pressure will have a defined distribution over the length of the vehicle, i.e. from the bow to the stern [10]. It is also expected that the pressure will depend on the position along the width of the vehicle, i.e. the distance between the starboard and port of the vehicle. To capture these length and width-wise pressure distributions, two types of pressure transducers are used, as shown in Figure 2-10.

Figure 2-10 Low and high speed pressure transducers used to capture air pressure

The low sample rate pressure transducer, i.e. measuring air pressure at 10 Hz, shown on the left, is a Gulf Coast Data Concepts USB pressure sensor, part number B1100-1. These sensors are a standalone system that are powered by a AA battery, each with its own internal memory, and each with a USB connection to be loaded to a computer after data acquisition. The high sample rate pressure transducer, i.e. measuring air pressure at 1 kHz, shown on the right, is an Omega pressure sensor, part number PX309-001G5V. The sensor is powered and the data is recorded by a laptop computer via the attached USB cable.

The on-site experiment saw the pressure sensors mounted to the track, i.e. at a stationary location, recording the pressure change as the train passed by. To replicate these conditions, a low sample rate sensor and a high sample rate sensor were mounted on the ground and were at approximately mid-span width-wise of the vehicle, i.e. about half way between the port and starboard of the automobile that passed over. It was not trivial to aim the automobile to pass over a series of sensors mounted width-wise, so the hypothesis of a uniform width-wise pressure distribution was not tested before the on-site experiment. However, with the two different pressure sensors mounted on the ground, the length-wise pressure distribution was tested and the results are shown in Figure 2-11.

Figure 2-11 Pressure distribution in stationary reference frame for car pass

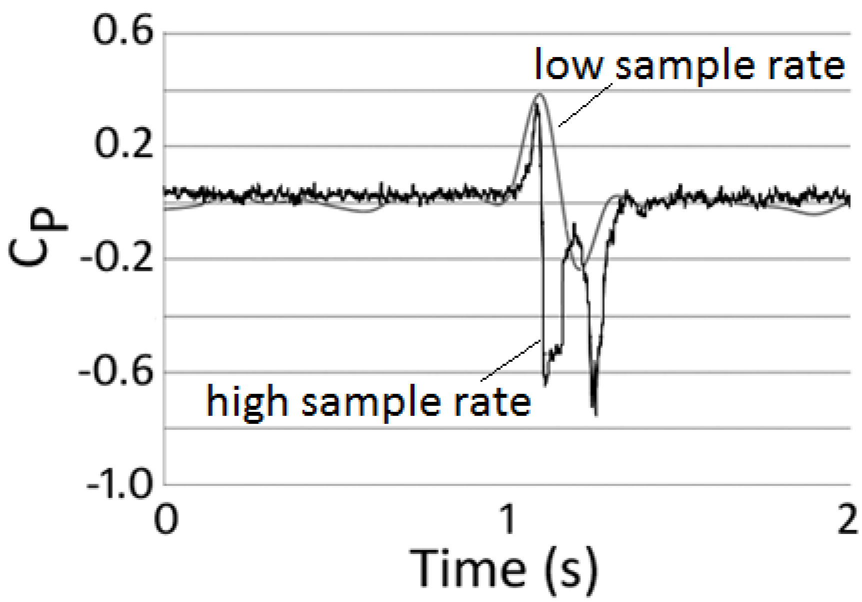

Figure 2-11 shows the coefficient of pressure C_P plotted over time t. The high sample rate 1 kHz signal, shown as the darker black line, was superimposed on the low sample rate 10 Hz signal, shown as the lighter, smoother grey line. The coefficient of pressure C_P is the ratio of measured pressure P to dynamic pressure $P_\infty = \frac{1}{2}\rho v_{fs}^2$, as shown in equation 2.4.

$$C_P = \frac{P}{1/2\,\rho v_{fs}^2} \tag{2.4}$$

It is clear that both sensors are able to capture the initial impulse in pressure when the automobile first approaches the location of the sensors, but it is also evident that the lower sample rate sensors do not capture the complete trend of the suction, i.e. negative value of pressure coefficient C_P, as the high sample rate sensor shows more definition in the shape of the distribution. Thus, it was determined based on this type of test that the lower sample rate pressure sensors would serve the purpose for measuring the magnitudes of the width-wise pressure distribution for the on-site testing, but that the output from the higher sample rate sensor would record the complete shape of the length-wise pressure distribution.

The on-site experimentation involves running the train by the pressure sensors with the train going both forward and backward. Figure 2-12 shows this type of test performed by two different types of automobiles. The solid lines represent a 2001 Toyota Celica GT. The dashed lines represent a 2001 Chrysler Neon LE. The pressure coefficient C_P is plotted against a dimensionless ratio of time $\frac{t}{\tau}$ where the characteristic time τ is the time it takes for the length of the vehicle to completely pass by the pressure sensor, i.e. the length divided by velocity. The Celica is 4.3 m (14.2 ft) in length. The Neon is 4.4 m (14.5 ft) in length. The minimum ground clearance for both vehicles is approximately 0.2 m (0.5 ft), each with similar underbody geometry. The vehicle speed was approximately 8.3 m/s for each run.

Figure 2-12 Pressure distribution for forward and backward automobile runs

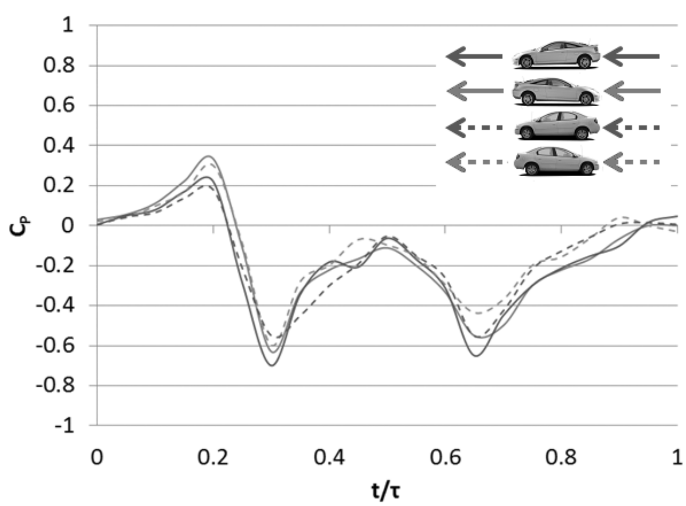

Starting at around 1 second in Figure 2-11, the air pressure activity becomes apparent. This is nearly simultaneous with the leading end of the vehicle passing over the pressure sensor. Thus, Figure 2-12 is essentially zoomed in to the section of Figure 2-11 between 1 and 1.5 seconds, taking that half second span as the characteristic time τ for the vehicle as it passes over the pressure sensor.

2.1.3 **Test Plan**

On-site testing was carried out in North Platte, Nebraska on June 4, 2014. One working day was allotted for experimentation. In this window, a locomotive and a single rail car were provided as an experimental apparatus. A crew, including an engineer and site charge hand, was provided to ensure site safety and to drive the locomotive. A stretch of uninterrupted track, long enough to accelerate and decelerate to the required speeds, was provided. Following the completion of all preliminary testing, a test plan was developed based on the estimations of duration of experimental setup, the duration of each experiment, and the most time-efficient order of experiments, ensuring that all important data points are completed first in the event of a failure within the system. Table 2.1 shows the experimental procedure performed. Two orientations for 'CTA system position' are listed – wheel center, and wheel edge. The wheel center orientation saw the train-mounted CTA system sensor mounted downwind of the wheel at the center of its width, and the wheel edge had the sensor closer to the edge of the wheel width in order to determine if there is a width-wise velocity gradient. The maximum train speed within the rail yard was 20 mph and the locomotive speed could be controlled by the engineer and recorded by its event recording system at an uncertainty of ± 0.5 mph. The tests listed in Table 2.1 are in order of priority, i.e. it was desired to capture the allowable speed spectrum as possible for both train directions first, before changing the orientation of the CTA system position. Each unique train speed provided an opportunity to prove that the results are scalable with velocity. Two train directions are listed – locomotive leading (bogie leading) and car leading (bogie trailing). Figure 2-13 shows the direction of the train for each orientation.

Table 2.1 Experimental test procedure

CTA System Position	Train Speed	Train Direction
Wheel center	5 mph	Locomotive Leading
Wheel center	5 mph	Car Leading
Wheel center	10 mph	Locomotive Leading
Wheel center	10 mph	Car Leading
Wheel center	15 mph	Locomotive Leading
Wheel center	15 mph	Car Leading
Wheel center	20 mph	Locomotive Leading
Wheel center	20 mph	Car Leading
Wheel edge	5 mph	Locomotive Leading
Wheel edge	5 mph	Car Leading
Wheel edge	10 mph	Locomotive Leading
Wheel edge	10 mph	Car Leading
Wheel edge	15 mph	Locomotive Leading
Wheel edge	15 mph	Car Leading
Wheel edge	20 mph	Locomotive Leading
Wheel edge	20 mph	Car Leading
Wheel edge	17.5 mph	Locomotive Leading
Wheel edge	17.5 mph	Car Leading
Wheel edge	12.5 mph	Locomotive Leading
Wheel edge	12.5 mph	Car Leading

Figure 2-13 Train direction with sensor location

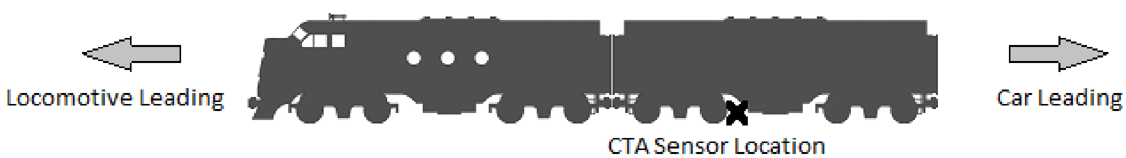

By reversing the train direction for each run, the same length of rail could be used in each run, meaning the location of the pressure sensors mounted to the ground did not need to change between tests. A sample experimental run is shown in Figure 2-14. In this run, the locomotive and rail car start at the east end of the track, accelerate to 20 mph and maintain the speed for several seconds, including passing over the location of the pressure sensor array marked at the center of the track length, before decelerating back to rest at the west end of the track.

Figure 2-14 Sample experimental run for train

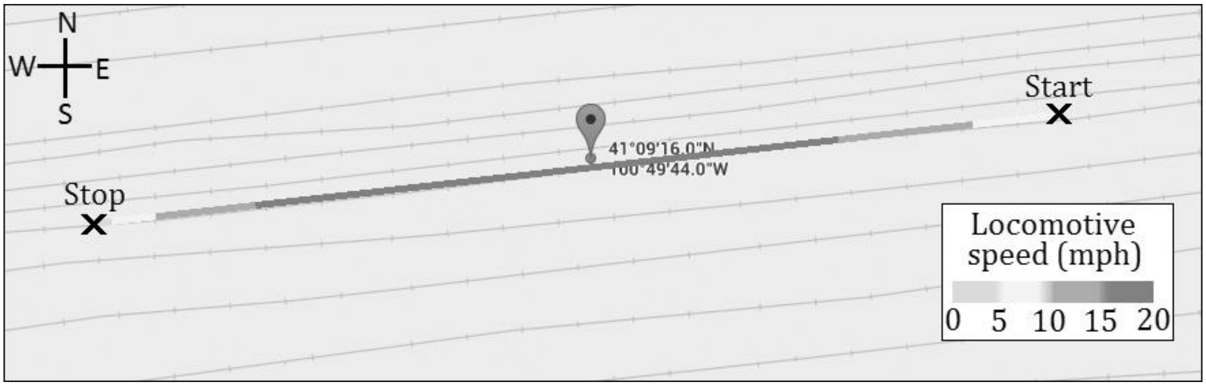

2.2 Monitoring Ambient Conditions

The ambient conditions were monitored using a Davis weather station, part number Pro2. The weather station measures ambient wind speed and air temperature. The assembled unit is shown in Figure 2-15. The conditions were recorded for each experimental run.

Figure 2-15 Weather station used to record ambient conditions

2.3 Measuring Air Pressure in the Reference Frame of the Track

It was determined during preliminary testing that the high sample rate 1 kHz pressure transducer was able to capture data points crucial to fully explaining the length-wise pressure distribution of the passing vehicle. It was then decided that the most important point along the track width was at the rail itself as that is where the friction modifier is deployed. Thus, the high sample rate 1 kHz pressure transducer was mounted near the rail, 0.17 m from the center of the rail as shown in Figure 2-16.

Figure 2-16 Location of pressure transducers

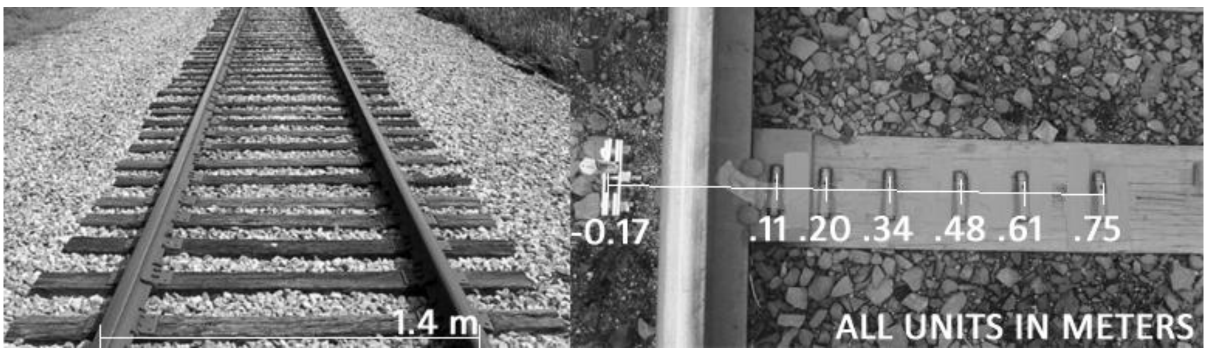

The array of low sample rate 10 Hz pressure transducers were then mounted in line with the high sample rate 1 kHz pressure transducer throughout the track width, ranging from 0.11 m to 0.75 m from the rail, as shown in Figure 2-16. As the entire width of the track is 1.4 m, the array of low sample rate 10 Hz pressure transducers captured half of the width of the track. It is assumed that, due to the symmetry of the train, the pressure distribution would also be symmetrical over the width of the track. All of the pressure sensors were mounted to the ground approximately half way between the start and finish line of each test run, as shown by the marker in Figure 2-14.

2.4 Measuring Air Velocity in the Reference Frame of the Train

Air velocity in the reference frame of the train was measured at 1 kHz using the CTA system. The system was mounted to the rail car and the laptop was fastened on the walking platform of the locomotive to provide easy access to start and stop data acquisition between runs. The mobile power source was also mounted on the locomotive, providing power to both the laptop at low charge and the CTA system for the duration of the experimentation. The cables were fastened to the edges of the locomotive, fed from the locomotive to the rail car, and fastened to the edge of the rail car, connecting the CTA system sensors to the bracket. The bracket, shown in Figure 2-17, was designed completely using three-dimensional computer aided drawing (CAD) software using commercially available parts to allow maximum flexibility when on-site. A test rig was available for a sample fitting of the bracket, but the actual on-site geometry was best replicated using CAD. The assembly made use of a 45 degree angle bracket to best insert the CTA system sensor into the flow for minimum aerodynamic interference from any bluff body that is not a typical component of the train, and to allow the sensor to be closer to the wheel. Figure 2-18 shows the location of the CTA sensor tips in relation to the wheel and rail when mounted on the bracket.

Figure 2-17 Bracket used to mount hot wire anemometers to train

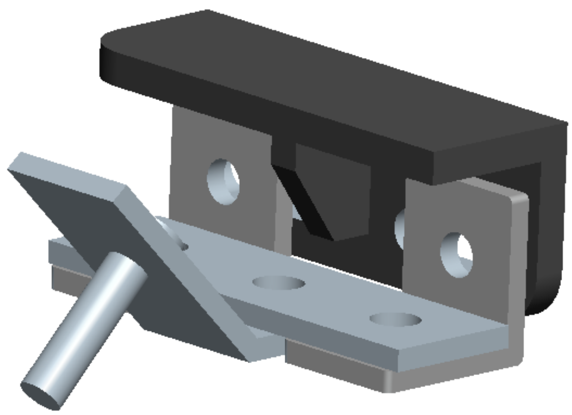

Figure 2-18 Location of hot wire anemometers

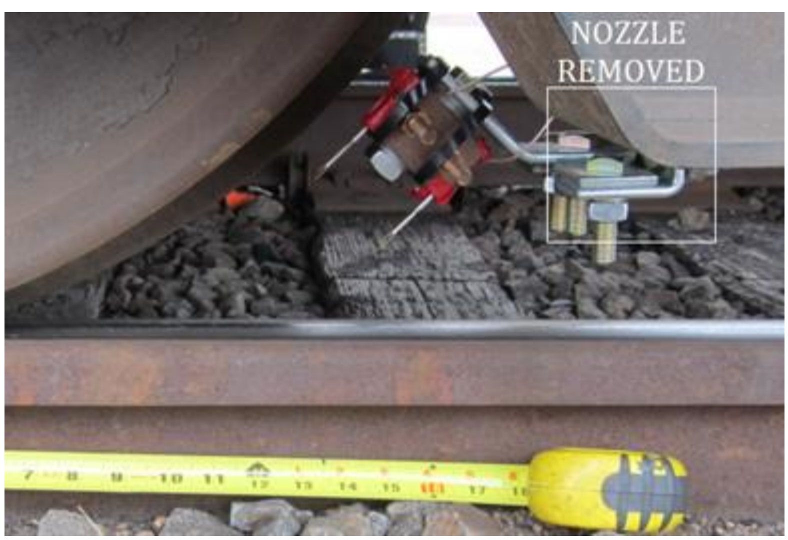

3 FREIGHT TRAIN TESTING

For each of the test cases in Table 2.1, the air pressure was evaluated throughout the train length and track width in the stationary ground reference frame. The results are in section 3.1. The air velocity was evaluated in the moving reference frame of the train. The results are in section 3.2. Figure 3-2 shows a snapshot of both systems in action, i.e. the CTA system air velocity sensors, mounted to the train, passing over the pressure transducers, mounted on the tracks.

Figure 3-1 Train passing by location of pressure transducers

3.1 Pressure Distribution

Air pressure was measured at 1 kHz by a high sample rate pressure sensor 0.17 m from the rail. Pressure was measured at 10 Hz by an array of low sample rate pressure sensors spread at locations between 0.11 and 0.75 m from the rail, representing approximately half of the rail width. Plotting the pressure coefficient C_P, i.e. the dimensionless ratio of measured pressure P to dynamic pressure P_∞, against dimensionless time, i.e. the ratio of the vehicle length, or characteristic length L, to the vehicle velocity v passing with time, it was found that the car leading orientation produced suction spikes much greater than the locomotive leading orientation. The locomotive leading results are shown in Figure 3-2 and the car leading results are shown in Figure 3-3. This is an unexpected result as the locomotive leading orientation contains geometry that is closer to the ground than the car, which sits higher off of the ground and farther away from the track. With a body closer to the ground, i.e. the locomotive compared to the car, a Venturi-governed flow would produce an effect with higher velocity and lower pressure, i.e. a negative dimensionless pressure with a larger magnitude, but this was not the case, indicating that the Venturi component was not strong compared to other driving conditions. When compared to the results from an automobile pass as in Figure 2-12, it is apparent that the pressure distribution profiles are different for the two vehicle types. The automobile passes tend to have a secondary suction spike near $\frac{t}{\tau} \approx 0.7$ whereas the longer trains tend to have an initial suction spike but no secondary spike – just recovery back to a pressure coefficient of zero.

Figure 3-2 Locomotive leading length-wise pressure distribution

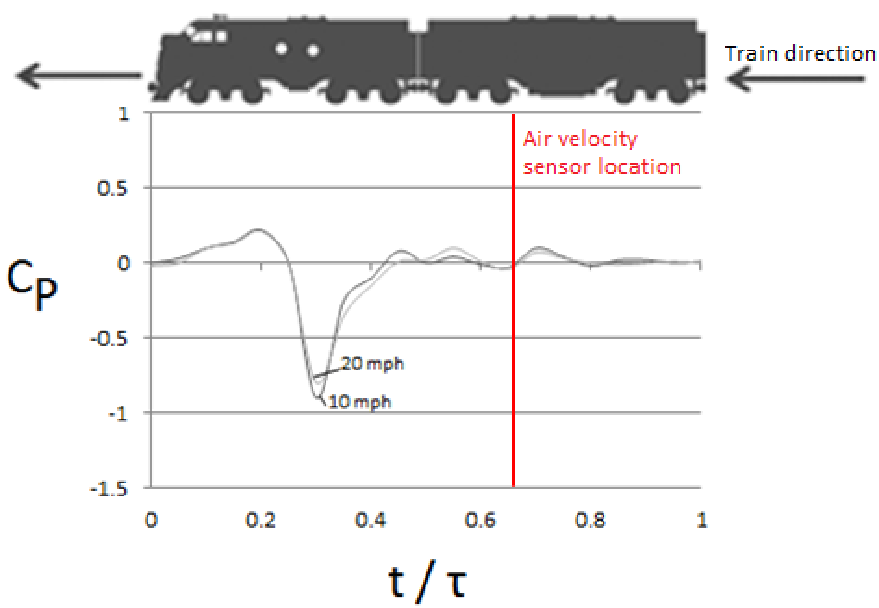

Figure 3-3 Car leading length-wise pressure distribution

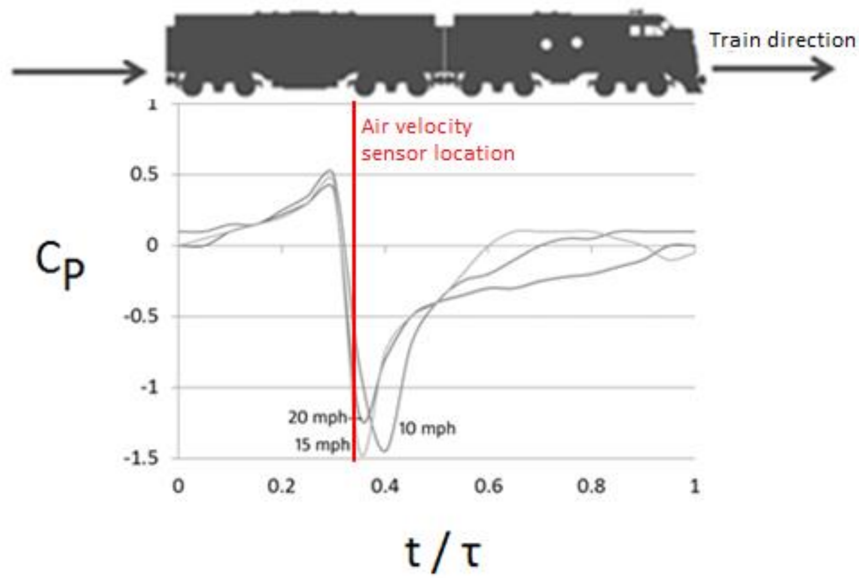

Figure 3-4 Track width-wise pressure distribution

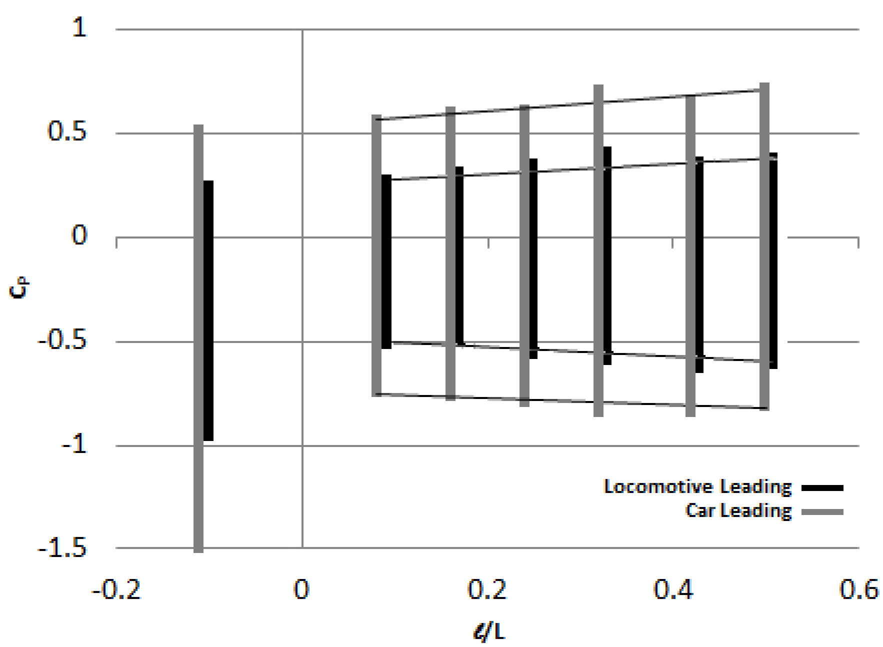

The track width-wise pressure distribution was also evaluated using the low sample rate 10 Hz pressure transducers, and the results are shown in Figure 3-4. In this plot, the peak positive and negative pressure coefficients, C_p, are plotted against sensor position l relative to the track width L with the position of the rail defining the location $l = 0$. The bar limits show the maximum and minimum pressure coefficient measured for each train direction, with positive pressure coefficients showing the magnitudes of the initial pressure impulse, and negative pressure coefficients showing the magnitudes of the suction spikes.

It was hypothesized that the pressure variation across the width of the track would be small. The slopes, $\Delta C_p / \Delta(\frac{l}{L})$, for the pressure impulses are 0.35 for car leading and 0.26 for locomotive leading. For the suction spikes, the slopes are 0.16 for car leading and 0.23 for locomotive leading. Both slopes are indeed reasonably small, though not negligible, implying that there is a modest width-wise variation in pressure at the train undercarriage. For example, for the car-leading configuration the peak positive pressure at the track centerline (0.75) is about 25% greater than near the rail (0.6). Similarly, for the same configuration the peak negative pressure at the track centerline (-0.8) is about 15% larger in magnitude than the peak negative pressure near the rail (-0.7).The low sample rate 10 Hz pressure transducers were able to capture nearly the same maximum positive pressure impulse as the high sample rate 1 kHz sensors. The left-most set of data points on the plot are read from the high sample rate 1 kHz sensor, and all points to the right of the y-axis are read from the low sample rate 10 Hz sensors. However, the magnitude of the maximum suction spikes, i.e. when the pressure coefficient is most negative, is not captured by the low sample rate 10 Hz sensors, implying that these spikes in suction happen over a short period of time. This phenomenon is true for both the locomotive leading orientation, shown in black, and the car leading orientation, shown in grey.

3.2 Velocity Distribution

Air velocity was measured at 1 KHz by the CTA system mounted on the train near a wheel. The free stream velocity, i.e. the velocity of the locomotive (neglecting cross wind effects), was measured using the event recorder data and time-synched with the on-board sensors. The raw data measured locomotive speed in miles per hour with accuracy ±1 mph at 1 Hz. The event recorder also produces location data to compare with time stamping to determine the time at which it passes over the pressure sensors mounted to the fixed location on the track. Figure 3-5 shows a typical velocity curve logged by the locomotive event recorder.

Figure 3-5 Raw data from locomotive speed event recorder

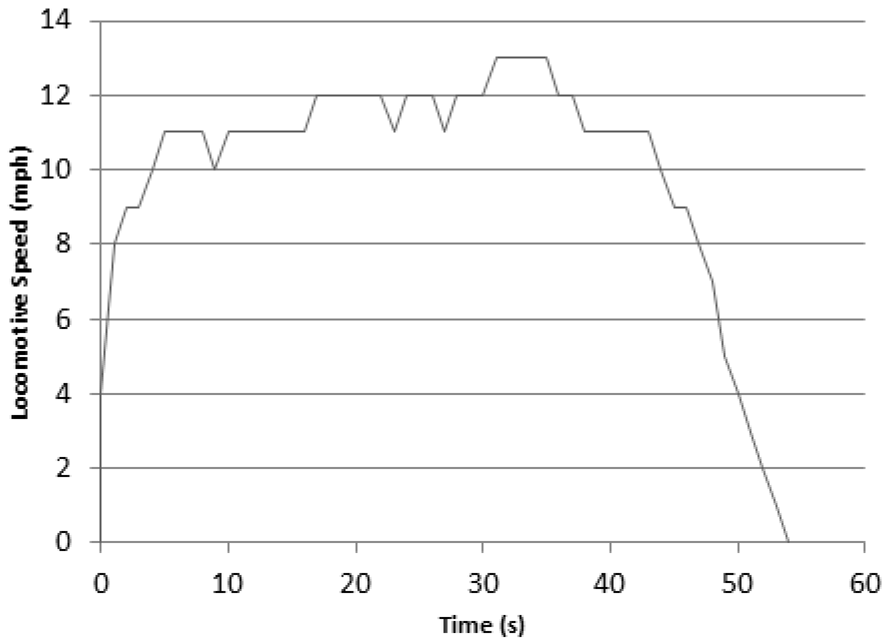

Figure 3-6 shows the dimensionless relative air speed, i.e. the ratio of the measured air speed to the train speed, for each of the test cases in Table 2.1. Meteorological station measurements showed that the wind was blowing close to 4 ms^{-1} (9 mph) for most of the day, and it was found that the relative air speed near the wheel contained significantly more uncertainty and usually an abnormally large magnitude when the train speed was equal to or less than the ambient wind speed. It was found that when the train moves at a speed greater than the ambient wind speed, the driving factor in the air speed at the wheel is the speed of the train. The collapse of the averaged relative speeds to a line at demonstrates that the results are scalable with velocity when the train is moving faster than the cross wind speed. Ignoring the points below the ambient wind speed, i.e. the most unpredictable and uncertain data points shown with large range in the whiskers, it was found that the time-averaged air speed at the wheel was 38% of the train speed for the car leading orientation, as shown in grey, and 29% of the train speed for the locomotive leading orientation, shown in black. These values are consistent with Baker's [3] measurements with pitot-static tubes.

Figure 3-6 Air velocity close to the wheel relative to the speed of the train

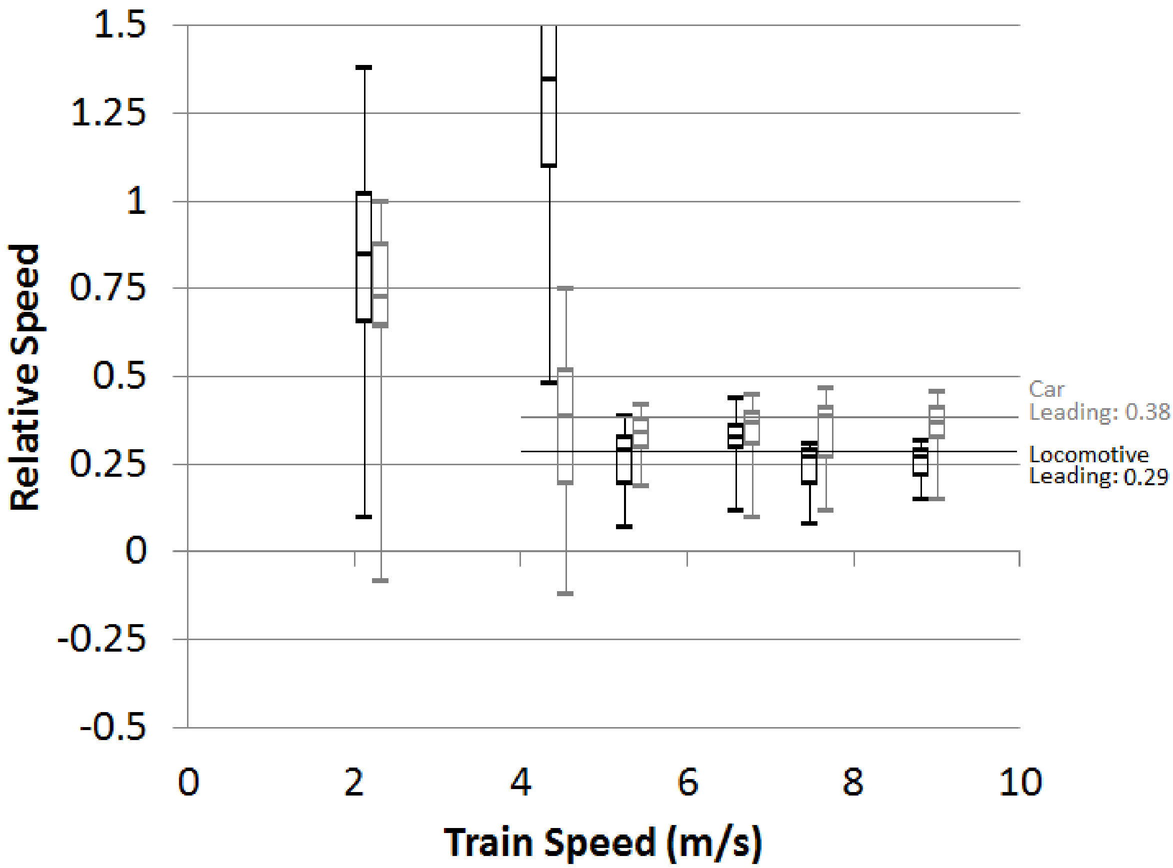

The flow for the locomotive leading orientation can be compared to flow around an isolated cylinder as in section 2.1.2. The car leading flow is more complex but has similarities to turbulent Couette flow in that the flow can be considered to be driven by the bottom face of the rail car moving over the stationary ground.

The turbulence intensity, i.e. the ratio of the root mean square variation in velocity to the average velocity, was found to be high – above 8% – and was generally higher for car-leading relative to locomotive-leading configurations. The turbulence intensity tended to drop as the average train speed increased, due to diminishing cross wind effects, as seen in Figure 3-7.

Figure 3-7 Turbulence intensity for air flow at the wheel of the train

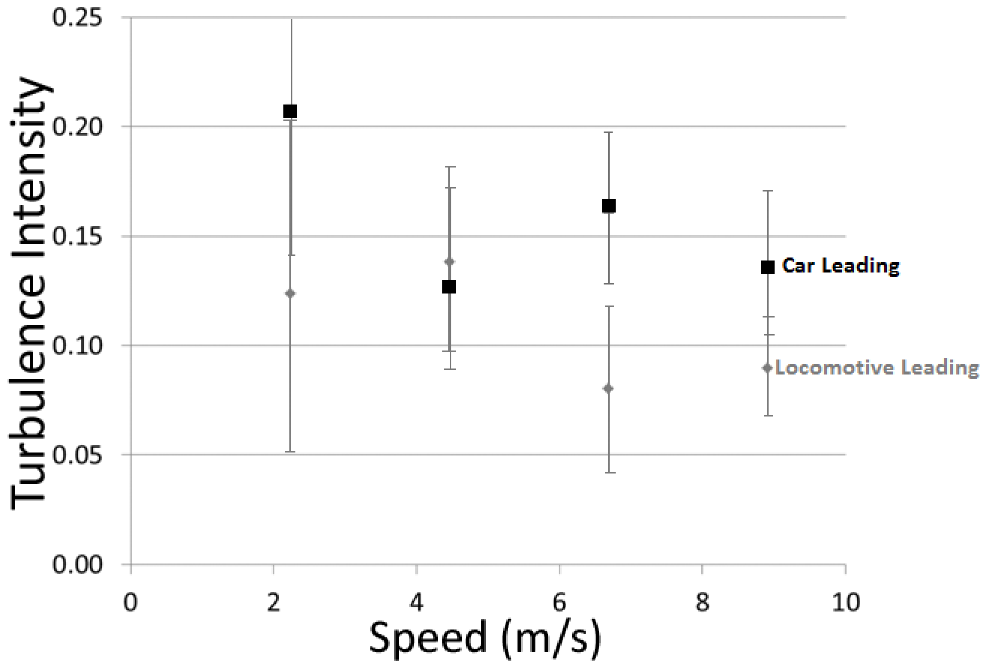

Performing a fast Fourier transform through the air velocity data showed the dominant oscillatory frequencies. When compared to a von Karman vortex street behind a cylinder as in section 2.1.2, the results showed predictable frequencies when considering the width and diameter of the wheel for the locomotive-leading orientation as shown in Figure 3-8. The frequencies are predictable by equation 2.3. For Figure 3-8A, knowing $v = 8.9\ \frac{\mathrm{m}}{\mathrm{s}}$ and $0.18 \leq St \leq 0.22$, the spike at $f = 11$ Hz as found in the spectral analysis, equation 2.3 implies a characteristic length of 0.14 m $\leq D \leq$ 0.18 m, which matches with the width of the wheel (0.14 m). For the spike at $f = 2$ Hz, equation 2.3 implies a characteristic length of 0.80 m $\leq D \leq$ 1.0 m, which matches with the order of the diameter of the wheel (1.0 m). Similar analysis is possible for Figure 3-8B to predict the same characteristic lengths.

Figure 3-8 Spectral analysis for locomotive leading air velocity data

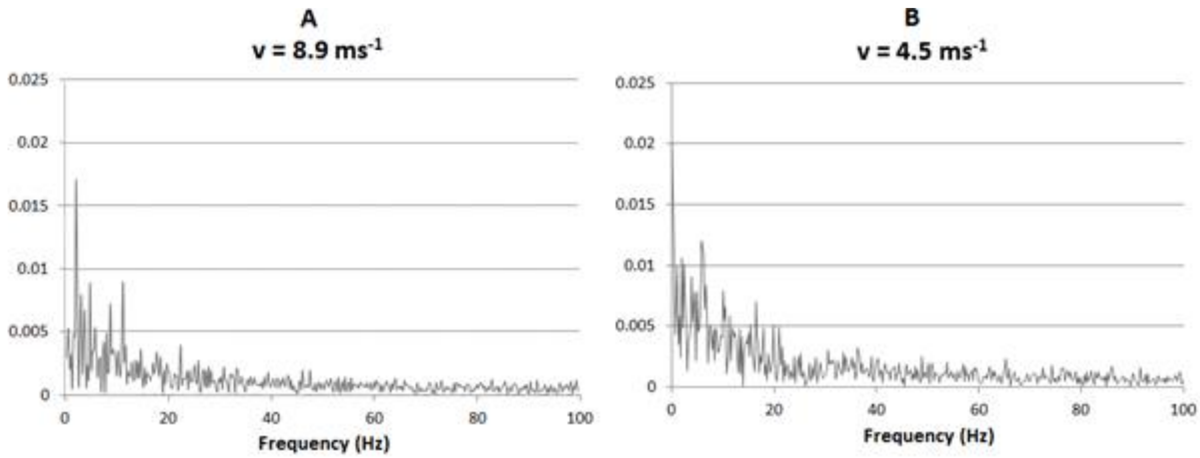

For the car-leading orientation with no immediately upwind geometry there were less distinct peak frequencies. As in Figure 3-9A, for the spike at $f = 7$ Hz, equation 2.3 implies a characteristic length of 0.23 m $\leq D \leq$ 0.28 m, which loosely matches with the width of the bracket that the sensors were mounted on. Similar analysis is possible for Figure 3-8B to predict the same characteristic lengths.

Figure 3-9 Spectral analysis for car leading air velocity data

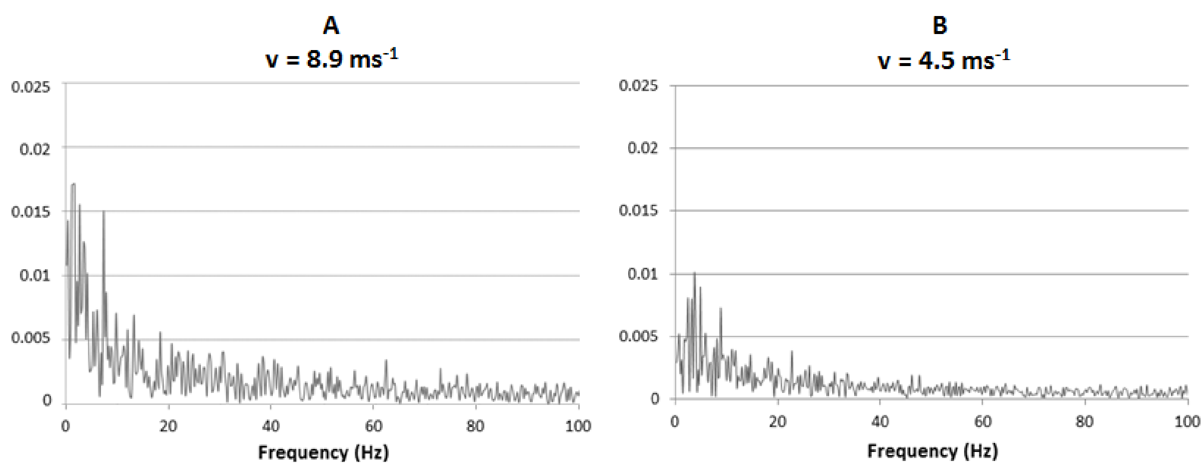

The Strouhal number St, also tended to drop slightly with increasing velocities as shown in Figure 3-10. This behavior is consistent for increasing Reynolds number with comparable geometry as in Ahlborn [8]. In this plot, the Strouhal number is plotted against dimensionless rotational velocity $\propto$ (defined in equation 3.1) i.e. the ratio of the rotational velocity, the product of the diameter D and rotation speed ω, and the velocity at the wheel v.

$$\propto = \frac{D\omega}{2v} \tag{3.1}$$

Figure 3-10 Strouhal number compared to rotational velocity

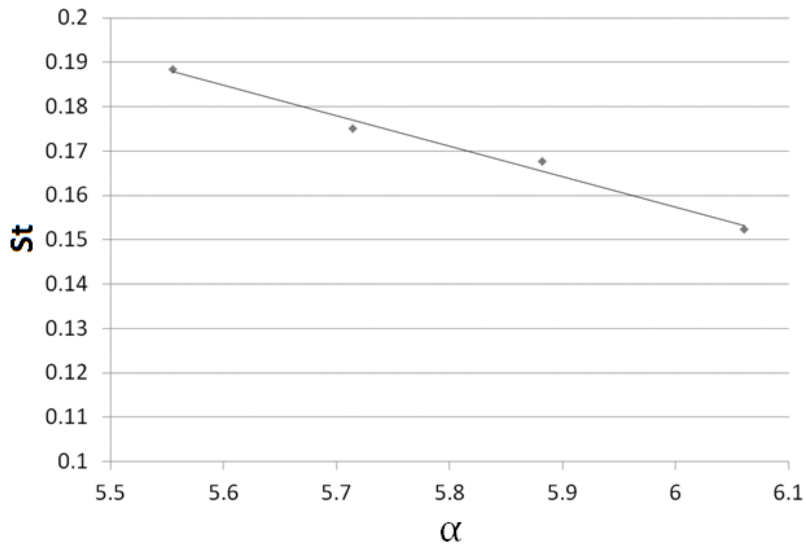

3.3 Statistical Analysis

The air velocity data points were collected at 1 kHz over multiple runs at different speeds and train directions, and were compiled and analyzed to further understand the flow characteristics. Particularly for the lower speed conditions, additional data was available when considering some of the data points from the higher speed tests when the train was in transition between rest and the operating speed.

After collecting the data points and sorting into bins, the probability for the locomotive leading direction, the air speed downwind of the wheel, is presented in Figure 3-11 for each of the train speeds recorded. It is immediately apparent that, in general, as the train speed increases and becomes large compared to ambient wind speeds, the standard deviation and variance of the data decreases. For the case of 5 mph locomotive speed, the effects of the cross winds were strong enough to cause a great enough variance to remove any obvious normal distribution. Each of the datasets with locomotive speeds equal to or greater than the cross wind speeds display similar mean values, with the exception of the 15 mph case, where the mean value appears to be an outlier. This is attributed to the gusty wind conditions during one of the two runs collecting data at 15 mph. In contrast with the 5 mph cross wind effects, the wind gusts present at the 15 mph condition were not consistently present throughout the entire duration of the experiment.

Another feature that is visible is the bimodality of the data. Particularly as the standard deviation and variance decreases, or as the train speed increases, two peaks begin to appear and form bimodal air velocity distributions. Due to the vortices shed by the wheel immediately upwind of the air velocity sensor, it is expected that a second mode will be present in the velocity distribution [11].

Figure 3-11 Probability for locomotive leading air velocity data points

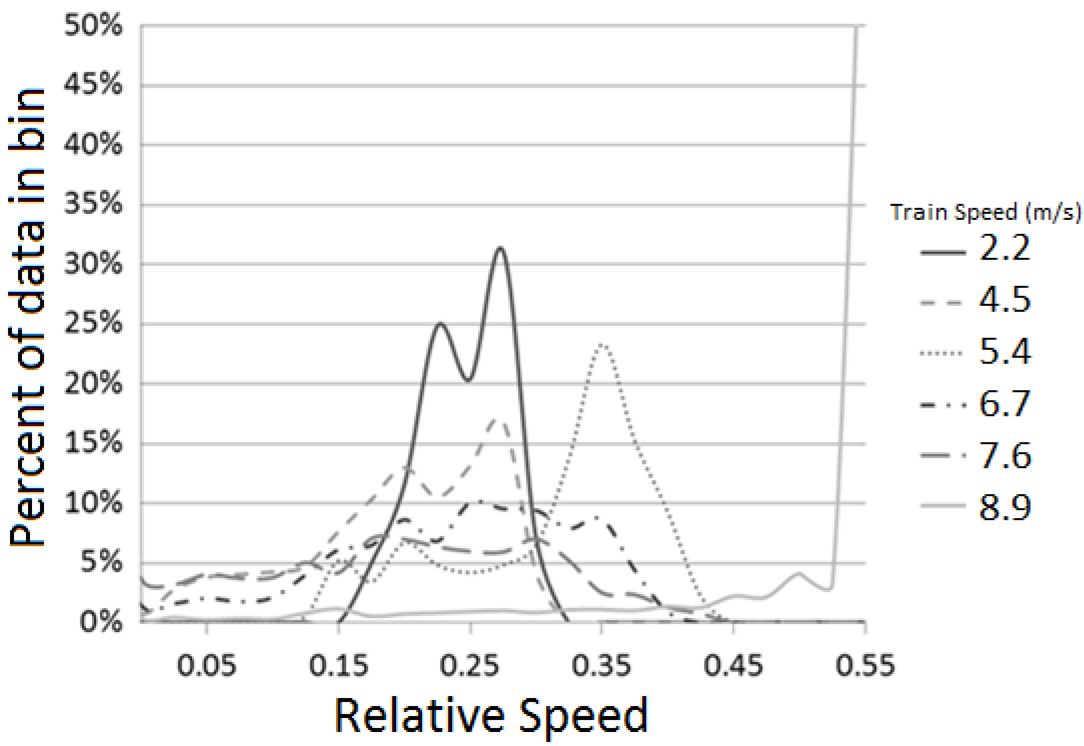

For the car leading train direction, the air speed upwind of the wheel, Figure 3-12 shows the probability distribution for the air velocity data.

As was observed in the locomotive-leading probability distributions, in general, as the train speed increased, the standard deviation and variance of the data decreased.

Unlike during the locomotive leading tests, there were no outliers due to gusty wind conditions as all train speed results displayed similar mean values. Also contrasting the locomotive leading probability distributions is the normality of the data. Because there were no major immediate upwind bodies, there was less vortex shedding activity and thus less bimodality.

As was discovered in section 3.2, for the locomotive leading direction, the mean value for each of the train speeds, save for the 15 mph outlier condition, was 27 to 29 percent of the train speed. For the car leading direction, the mean was 35 to 39 percent of the train speed.

Figure 3-12 Probability for car leading air velocity data points

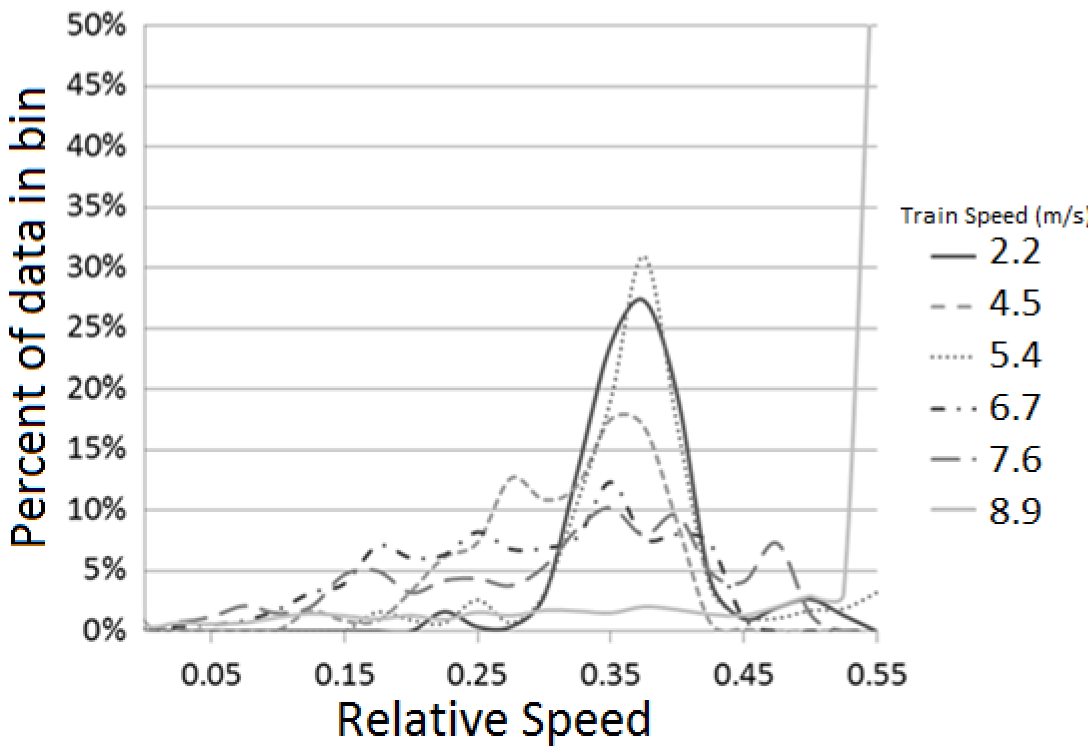

Plotting the mean points for each of the train speeds in each direction shows how the resulting air velocities scale with train speed. Due to the large variance and standard deviation, data points with locomotive speeds of less than 5.4 ms^{-1} (12 mph) were omitted completely. Simply plotting the mean values resulted in a reasonable linear fit through the origin with a correlation coefficient of 0.55 for the bimodal locomotive leading direction and 0.68 for the normal car leading direction. To improve on this data, outliers from each data set, i.e. data points that reside greater than two standard deviations from the mean, were removed. As well, the two modes were evaluated individually for the locomotive leading data. The resulting plot is shown in Figure 3-13.

Figure 3-13 Linearity of air velocity data with outliers removed

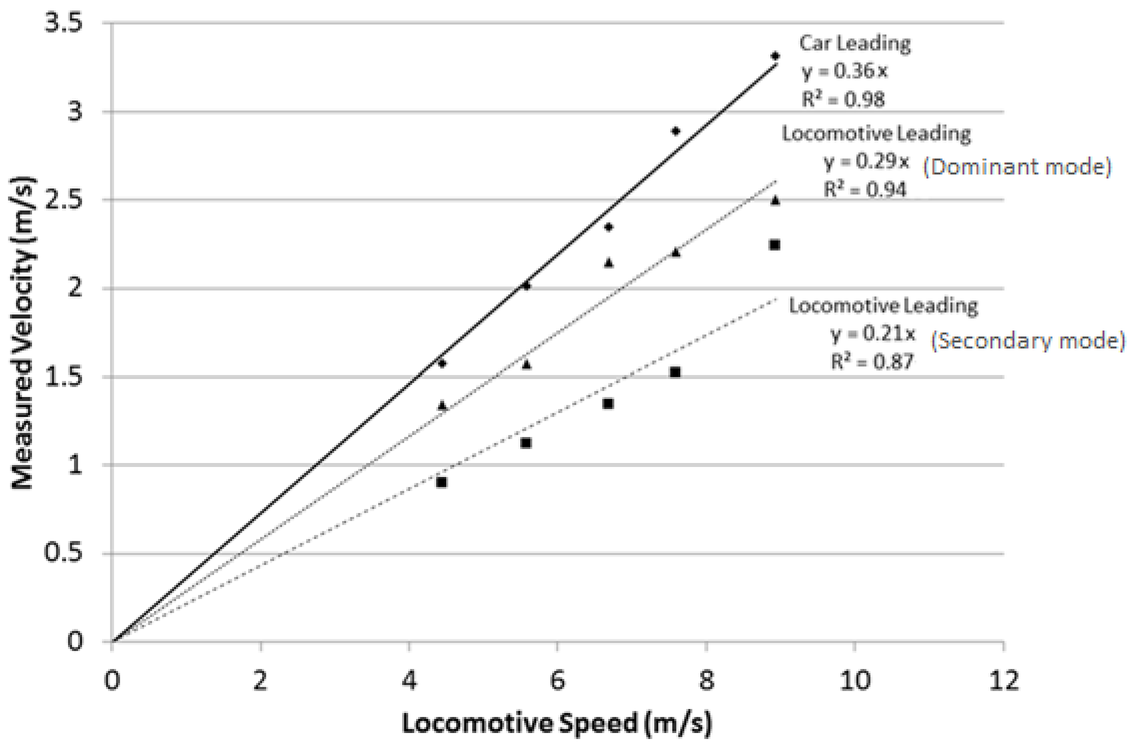

Removing the outlier data points results in data with a much better linear fit and a minimal change to the mean values. For the car leading direction, the correlation coefficient increases from 0.68 to a near perfect 0.98. For this direction the mean air speed measured in the frame of reference of the train was 36% of the train speed (i.e., in the frame of reference of the ground the mean speed was 64% of the train speed). For the locomotive leading direction, the dominant mode, i.e. the mode closest to the mean, saw a correlation coefficient of 0.94 and a mean value of about 30% of the locomotive speed. The second of the two modes, i.e. the mode caused by the vortices shed by the wheel upwind, saw a correlation coefficient of 0.87 and a mean value of about 20% of the locomotive speed. From this analysis, it can be concluded that the outliers, suspected to be present due to gusts of wind, tend not to bias the mean values but do tend to slightly scatter the results.

4 COMPUTATIONAL MODEL

To supplement the experimental aerodynamic data, a computational model was constructed. The model is intended to predict air velocity values at other locations of interest where no sensors were present. The model is also intended to confirm that the presence of the bracket holding the hot wire anemometers did not significantly impact the results. The experimental results were used to validate some predicted values and thus increase the confidence of the rest of the predictions.

4.1 Setting Up Simulation of Experimental Conditions

Figure 4-1 shows a simplified schematic of the experimental aerodynamic conditions. The velocity sensors were mounted to the moving vehicle, thus all measured velocity values were in the reference frame of the moving train. In this reference frame, the underbody is stationary, the rail and ground moves at the speed of the train, and the wheel rotates in the direction indicated. In a stationary reference frame, this configuration represents the train moving from left to right.

Figure 4-1 Simplified experimental environment to perform simulation

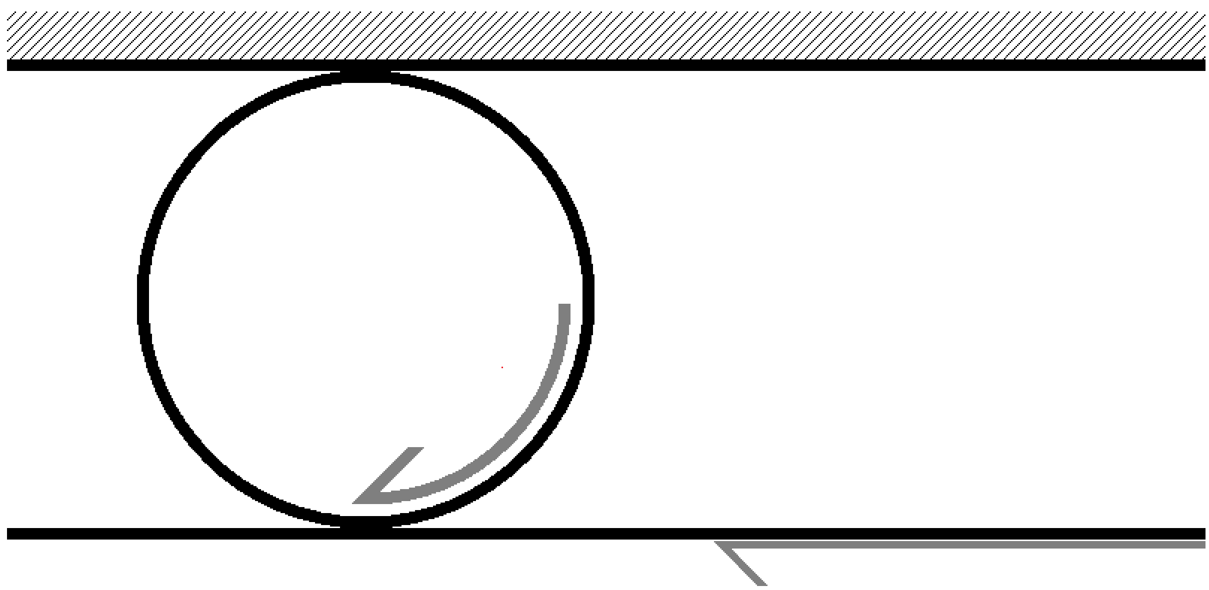

This simplified case itself has resemblance to a Couette flow. When considering the car leading direction, i.e. when the rotating wheel is downwind of the area of interest, the simplified, two-dimensional flow can be characterized by a stationary plate, represented by the bottom of the train, and a moving plate driving the flow, represented by the moving ground.

When considering the locomotive leading direction, as was discussed in section 3.2, the flow is analogous to flow behind a cylinder. The flow is more complicated due to the rotation of the cylinder, but the effects of the rotation on the downwind velocity profile were thought to be minimal at the location of the sensors during experimental testing as the results agreed with Baker’s mean results [3].

Based on the diagram in Figure 4-1, a three dimensional computational model was defined. The model is a wind-tunnel style rectangular prism, with a wheel located at the center length-wise and width-wise. The model was approximately three wheel diameters in length, one diameter in height, and eleven wheel widths in width. These distance values were minimized during grid convergence to allow the usage of the finest mesh that the simulation machine could handle with converging residuals. For the flow close to the wheel down the centerline, it was taken that a model of this size would be sufficiently large to neglect wall effects. For simplicity of matching non-dimensional values to the experimental conditions, the geometry was all defined at full scale.

The inlet and outlet, i.e. the faces upwind and downwind of the wheel, were set with pressure boundary conditions as found in section 3.1. The adjacent faces were set with a symmetry boundary condition on the side representing the train, and an atmospheric pressure boundary condition on the opposite wall. The top face, a simplified train underbody, was set to a no-slip wall boundary condition with no velocity, to replicate the experimental conditions in the reference frame of the train. The bottom face was set to a no-slip wall boundary condition with a variable velocity that would drive the flow. The wheel faces, including two circular faces and the face along the perimeter, were all modelled with a no-slip wall boundary condition with a rotational velocity about the axis of the wheel. At the maximum radius, the rotational velocity multiplied with the radius matched the speed of the moving rail. The model is shown in Figure 4-2. The boundary conditions outlined above are illustrated in Figure 4-3.

Figure 4-2 Computational model to simulate experimental conditions

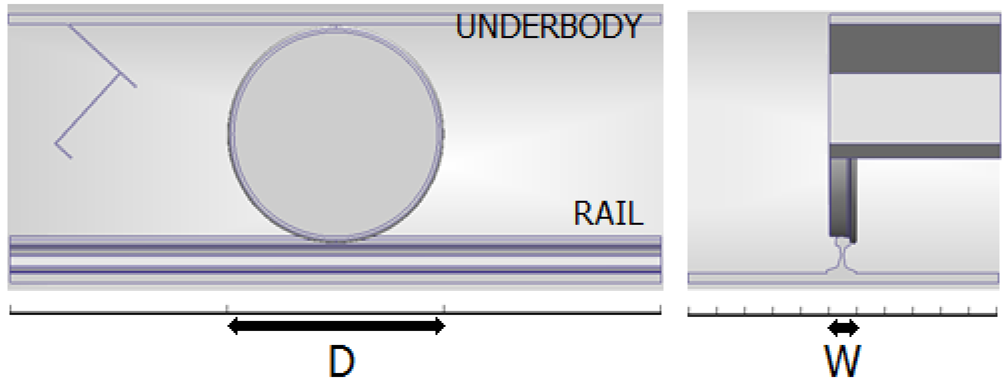

Figure 4-3 Boundary conditions to simulate experimental conditions

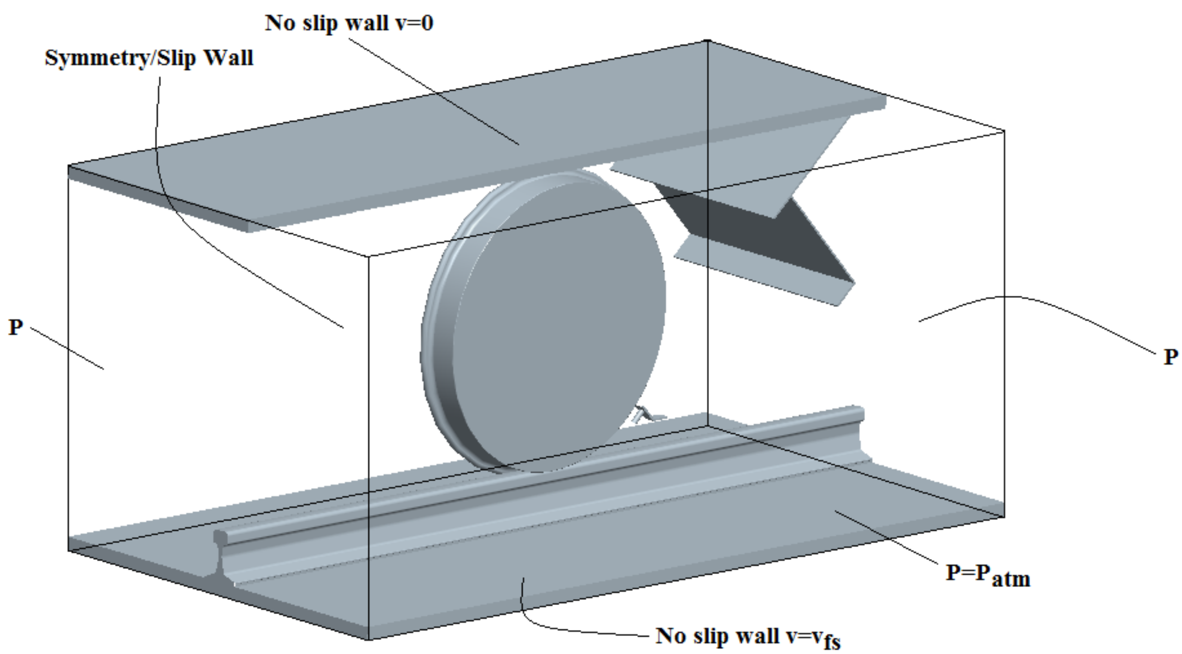

As shown in section 3.1, a pressure gradient exists along the length of the train. The magnitude of the pressure depends on the train direction. For the locomotive leading direction, the pressure gradient in the simulated region, i.e. from one wheel diameter upwind to one wheel diameter downwind, is on the order of $\frac{dP}{dx} = 0.5 \text{ Pa m}^{-1}$ for the most extreme experimental conditions, i.e. when v_{train}= 8.9 ms^{-1} (20 mph). Similarly, for the car leading direction, the pressure gradient is on the order of $\frac{dP}{dx} = 5.0 \text{ Pa m}^{-1}$. By assigning these differences in pressure to the inlet and outlet boundaries, noted with 'P' in Figure 4-3, a Poiseuille-like component is introduced to the previously defined Couette-like flow. Combined, the two components describe a velocity profile analogous to a Couette-Poiseuille flow. When $\frac{dP}{dx}$ is large, i.e. in the car leading direction, the Poiseuille component becomes more relevant as $v_{Poiseuille}$ approaches the magnitude of $v_{Couette}$. Thus, the pressure difference discovered experimentally cannot be ignored.

As shown in section 3.2, the flow was found to be highly turbulent with turbulence intensity values at a minimum of 0.10 for each test condition. A k-epsilon turbulence model was selected to simulate this type of turbulent external flow.

Using the experimental results for air velocity data, we have available the actual velocity value at a point 0.07 wheel diameters above the rail both upwind and downwind of the rotating wheel, each about 0.4 wheel diameters from the wheel center in either direction. With these known values, we can evaluate the simulation predictions.

Figure 4-4 shows the location of four simulated velocity distributions – two horizontal distributions, i.e. $v_{x,fixed\ y}$, and two vertical distributions, i.e. $v_{y,fixed\ x}$, each in the same position upwind and downwind of the wheel.

Figure 4-4 Diagram outlining position of velocity distributions

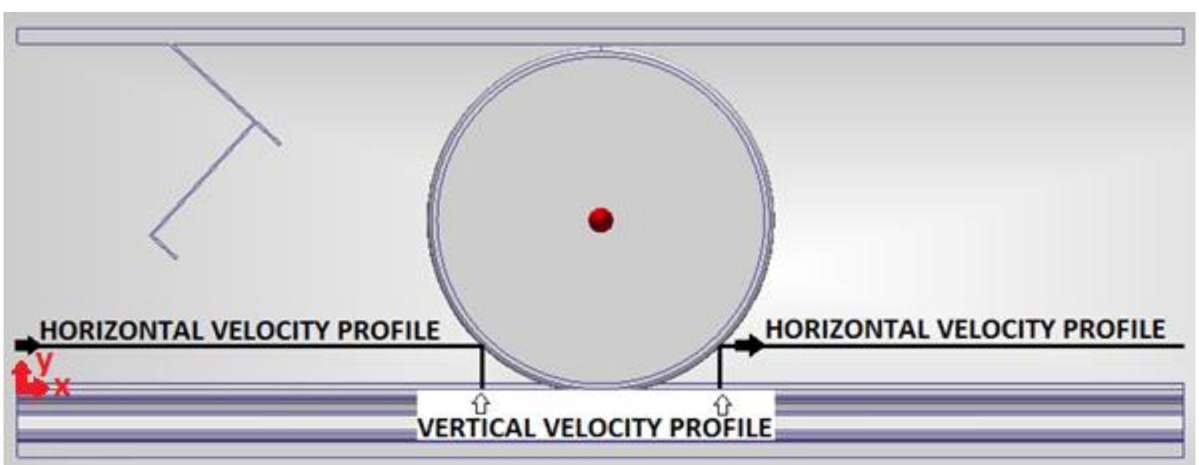

Grid convergence was performed to ensure the results were independent of the mesh. For each mesh trial, the simulation ran until the residual root mean square values converged to a value less than 10^{-3}. From there, the mesh was refined until reference velocity points changed by less than 1%.

4.2 Results of Simulating Experimental Conditions

The simulations characterized in section 4.1 were performed with and without the presence of the bracket geometry which held the hot wire anemometer in place. In all resulting plots, a black line representing the flow without the bracket is superimposed on a grey line representing the flow with the bracket. However, the difference between the conditions with and without the bracket is so minimal that the curves lie on top of one another. This indicates that the presence of a bracket did not have any impact on the velocity readings, i.e. the hot wire anemometer was aerodynamically isolated.

Figure 4-5 and Figure 4-6 show the simulated horizontal air velocity distribution for locomotive leading and car leading directions, respectively. Both of these velocity distributions are fixed at 0.4 wheel diameters away from the wheel center, upwind of the wheel in the case of the car leading direction and downwind of the wheel in the case of the locomotive leading direction. With this horizontal location fixed, the vertical range is then evaluated, i.e. from the rail, shown on the vertical-axis as 0, upward to the bottom of the wheel, shown on the vertical-axis as about 0.17. For both plots, the experimentally measured velocity is displayed by the circular point and is superimposed upon the rest of the simulated air velocity distribution.

For both vertical distributions from the rail upward, the simulated air velocity distribution closely agrees with the experimental points, i.e. the experimentally measured points lay on the simulated lines. Both distributions show a spike in air velocity near the top of the distribution, i.e. as the position is 0.15 diameters above the rail and above. This is due to the flow locally driven by the surface of the non-slip wheel surface. At the surface of the wheel, the absolute velocity is equivalent to the free stream velocity, which would be represented by a value of 1 on the horizontal axis. The plots display the vector sum of the air velocity components perpendicular to the hot wire anemometer, i.e. both in the down-wind and cross-wind directions. However, at higher locomotive speeds, it was shown that the effects of the cross-winds are minimal and the results are considered one dimensional in the down-wind direction. Thus, at the ground, or a position of zero diameters above the surface, the air velocity is 100% of the free stream velocity because, in this simulation and in this reference frame, the flow is being driven by the moving ground.

Figure 4-5 Vertical range of computed locomotive leading air velocity at 0.4 D downwind

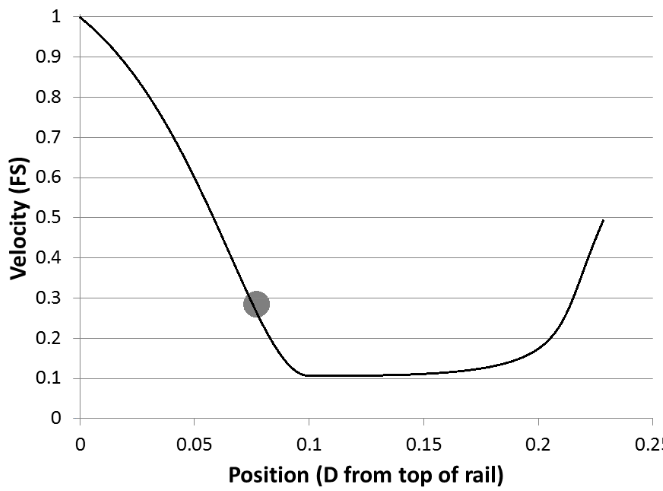

Figure 4-6 Vertical range of computed car leading air velocity at 0.4 D upwind

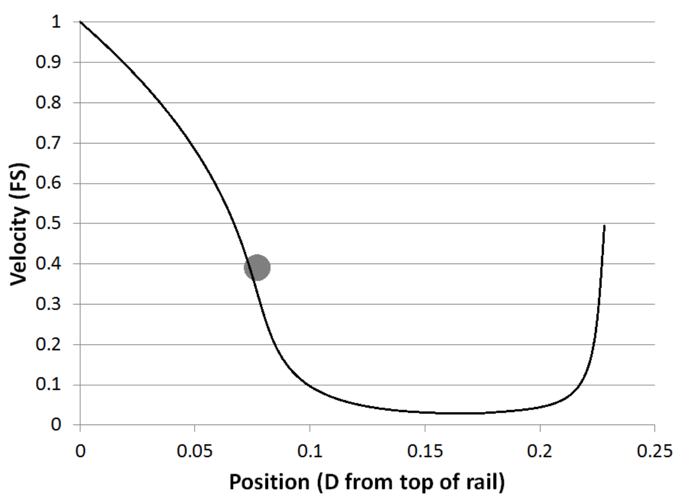

Figure 4-7 and Figure 4-8, similarly, show the simulated horizontal air velocity distribution with the superimposed experimental point. However, instead of fixing the horizontal distance from the wheel, it is now the vertical distance from the height that is fixed at 0.07 wheel diameters above the rail. The horizontal position is then shown on the horizontal axis with resulting velocity values on the vertical axis. There are no velocity values available less than 0.25 wheel diameters from the wheel center for either case, because that position would be inside the wheel.

As was the case with the vertical air velocity distributions, the experimental point agreed with the simulation for the horizontal air velocity distributions as well, with the experimental point appearing on the simulated line in both cases.

For the locomotive leading air velocity distribution, the flow is analogous to evaluating flow recovery behind a cylinder, i.e. the further downwind of the cylinder, or with increasing position, the flow recovers towards the free stream value. For the car leading air velocity distribution, the flow is analogous to evaluating flow as it approaches a cylindrical body. For both distributions, three-dimensional effects, i.e. uninterrupted flow at the extreme sides of the wheel width, cause the flow to recover at a faster rate. Also evident in both distributions is a spike in air velocity close to the wheel, shown at a position of 0.25 wheel diameters downwind of the wheel center for the locomotive leading direction, and 0.25 wheel diameters upwind of the wheel center for the car leading direction. This spike, as it was for the horizontal velocity distributions, is due to the flow being driven locally by the rotating wheel. However, the magnitudes of the velocity spikes are less than in comparison to the vertical air velocity distribution. This is because the velocity vector driven by the wheel at 0.07 diameters above the rail has a small component in the direction parallel to the track and a larger component in the direction perpendicular to the track. At zero wheel diameters above the track, i.e. at the bottom of the wheel, the velocity vector is parallel with the track and no component in the perpendicular direction would exist. At 0.5 diameters above the track, i.e. at mid span of the wheel, on either side the velocity vector is entirely perpendicular to the track and no component parallel to the track exists. Thus, at 0.07 diameters above the track, the velocity contributed by the wheel is mostly in the direction parallel to the track.

For all train speeds, i.e. to replicate the experiments with train speeds from 2.2 ms^{-1} (5 mph) to 8.9 ms^{-1} (20 mph), the resulting patterns were similar, as is expected with the results being shown to be scalable with velocity. However, it was discovered through simulation that the ‘boundary layer’, a loosely defined term referring to the distance required to become far enough from the rotating wheel where the wheel no longer was the primary flow driver, was in fact dependent on velocity, or more specifically, Reynolds number.

Figure 4-7 Horizontal range of computed locomotive leading air velocity at 0.07 D above the rail

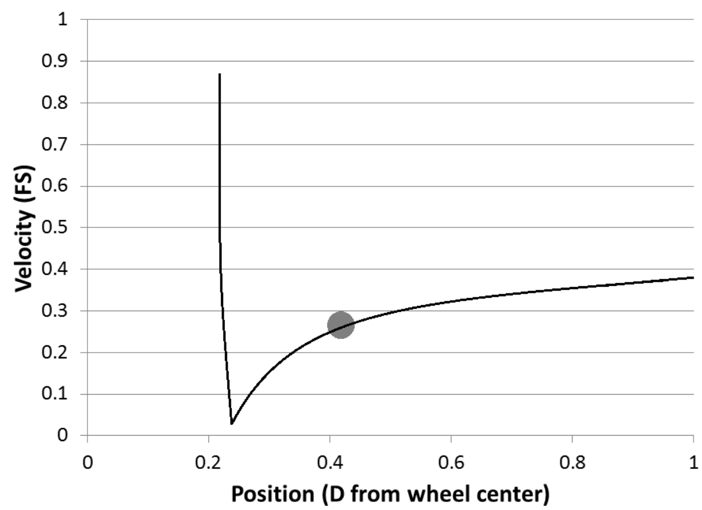

Figure 4-8 Horizontal range of computed car leading air velocity at 0.07 D above the rail

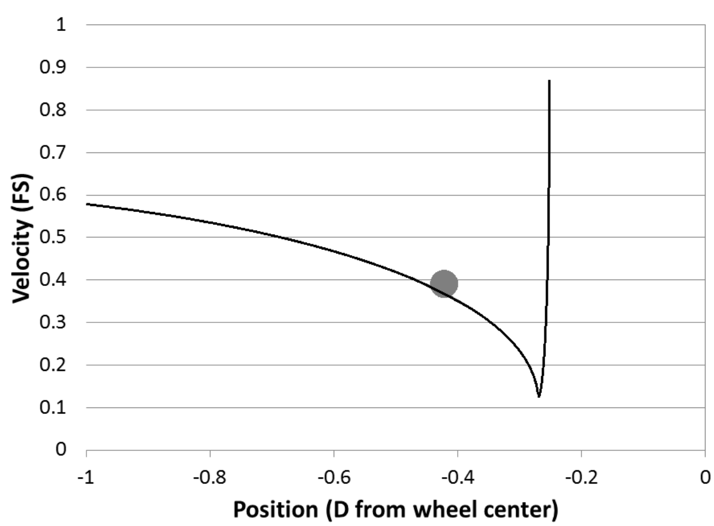

Figure 4-9 shows the dependency of flow recovery distance on Reynolds number. Plotted on the vertical axis is the flow recovery distance, normalized in terms of wheel diameters, required for the flow to recover to 95% of the free stream condition. The horizontal axis is a logarithmic Reynolds scale. A range of Reynolds numbers was plotted, from 3 x 10^5, corresponding to a locomotive speed of 5 ms^{-1} (10 mph), to 30 x 10^5, corresponding to a theoretical train speed of 60 ms^{-1} (135 mph).

The Reynolds number dependency appears to be evident up to about 10 x 10^5, at which point the flow recovery distance tends to converge to a similar distribution. This range of Reynolds number which defines the transitional region of boundary layer thickness is of the same order as the critical Reynolds numbers, 10^5 to 10^6, for cylinders [12].

Figure 4-9 Simulated flow recovery

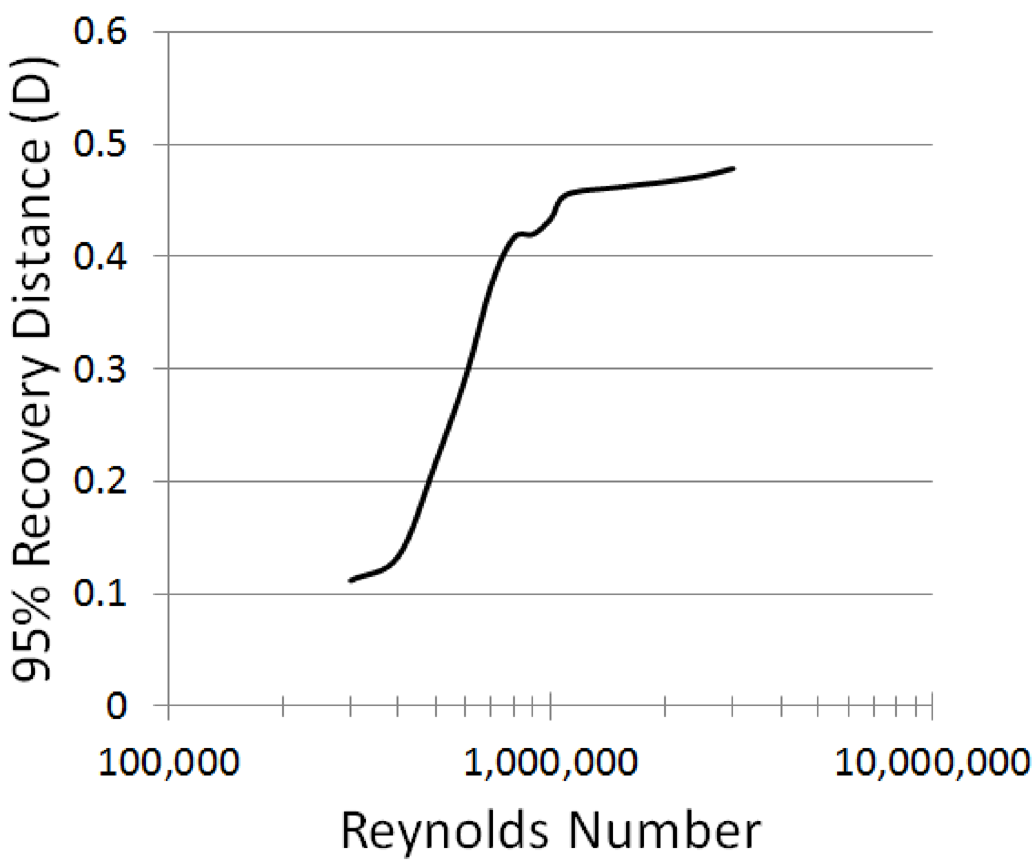

5 CONCLUSIONS AND RECOMMENDATIONS FOR FUTURE WORK

A full scale, experimental aerodynamic assessment of the underbody of a freight train was planned, scheduled and performed. Air velocity in the moving reference frame of the train was evaluated using fiber-film hot wire anemometers mounted on the train near the location of the wheel. Air pressure in the stationary reference frame of the ground was evaluated using two types of pressure transducers mounted on the tracks. Ambient conditions were monitored using a weather station.

The pressure distribution throughout the length of the train showed an initial positive impulse in air pressure when the leading end of the vehicle passed over the sensors before creating a negative pressure suction spike. The pressure then eventually recovered to zero gauge pressure by the time the trailing end of the vehicle passed. It was found that the magnitude of the initial impulse in air pressure was similar for the train travelling in either direction, but the magnitude of the suction spike was twice as large when the train travelled backwards, i.e. with the locomotive pushing the rail car. The pressure distribution throughout the width of the track was found to be approximately constant.

The air velocity at the wheel, at the location where spray nozzles are commonly mounted, was found to be 29% of the train speed with the locomotive leading, i.e. downwind of the wheel, but was found to be 38% of the train speed with the car leading, i.e. upwind of the wheel and without any bodies immediately upstream disrupting the flow. Particularly for the car leading case, this was in agreement with previous work performed on high speed trains. The effect of the cross winds were found to become much less significant when the train was travelling greater than the speed of the ambient wind. These magnitudes and the diminishing effects of cross winds at higher train speeds are the most important takeaways for understanding the input parameters for the liquid jet impingement problem.

The turbulence intensity was found to be very high, i.e. greater than 10% for most cases. The Strouhal number was found to decrease slightly with an increasing wheel rotational speed. With the sensor downwind of the wheel, spectral analysis produced predictable results based on flow around a cylinder in terms of vortex shedding frequency.

The standard deviation and variance was found to decrease as the train speed became larger than the ambient wind speeds, and the air velocities were shown to be scalable with velocity.

CFD calculations on a simplified geometry of the train undercarriage were shown to predict with reasonable accuracy air velocity values in the vicinity of where the experimental sensors were present. It was shown that, although the boundary layer from the rotating wheel was not a major flow driver, its thickness was dependent on Reynolds number for values in the range of the critical values for a cylinder.

It is recommended to perform further tests investigating the length-wise pressure distribution. Testing with automobiles showed a trend where there were two instances of suction, whereas with the longer trains, there was only one instance of suction before recovery to zero gauge pressure. It seems there may be a combination of length and speed in which the second instance of suction appears. It is also recommended to use the experimental data to validate simulations with additional geometry, such as the introduction of a wind skirt which could help shield friction modifying products.

BIBLIOGRAPHY

[1] Moulson J., 2011, “An Experimental Study of Liquid Jet Impingement on a Moving Surface: The Effects of Surrounding Air Pressure and Fluid Properties,” M.A.Sc. thesis, University of British Columbia.

[2] Sterling G.E.G., 2012, “An Experimental Study on Jet Impingement on a Very High Speed Moving Surface,” M.A.Sc. thesis, University of British Columbia.

[3] Baker, C., 2008, "The Flow around High Speed Trains," BBAA VI International Colloquium on: Bluff Bodies Aerodynamics & Applications, Milano, Italy, pp.1-34.

[4] Bradshaw P. and Huang G., “The Law of the Wall in Turbulent Flow,” Proceedings: Mathematical and Physical Sciences, 451(1941), pp.165-188.

[5] Kinzel M., Mulligan Q. and Dabiri J.O., “Energy Exchange in an Array of Vertical-Axis Wind Turbines,” J. Turbulence, 13(38), pp.1-13.

[6] Itoh, M., Tamano, S. Yokota, K. and Ninagawa, M., "Velocity Measurement in Turbulence Boundary Layer of Drag Reducing Surfactant Solution," Phys. Fluids, 17(7), pp.1-9.

[7] Elvidge, D., Cotter, J. and Eadie, D., 2012, LB Foster Friction Management, private communication.

[8] Ahlborn, B., Seto, M. L. and Noack, B. R., 2002, “On Strouhal number, drag, and vortex-street structure,” Fluid Dynamics Research 30, pp.379-399.

[9] Dantec Dynamics, 2012, “MiniCTA 54T42 Installation & User’s guide”.

[10] Marklund, J., 2013, “Under-body and Diffuser Flows of Passenger Vehicles,” Ph.D. thesis, Chalmers University of Technology.

[11] Konstantinidis, E., Balabani, S., Yianneskis, M., 2007, “Bimodal vortex shedding in a perturbed cylinder wake,” Physics of Fluids 19 (1) 011701.

[12] Holmes, J. D., 2001, “Wind loading of structures,” Spon Press Print ISBN: 978-0-419-24610-7.